ALL-ORDER POLARIZATION MODE DISPERSION SENSING AND COMPENSATION IN OPTICAL FIBER COMMUNICATION SYSTEMS

A Dissertation

Submitted to the Faculty

of

Purdue University

by

Li Xu

In Partial Fulfillment of the

Requirements for the Degree

of

Doctor of Philosophy

May 2010

Purdue University

West Lafayette, Indiana

This thesis is dedicated to my mother Maorong Zhang.

ACKNOWLEDGMENTS

Specially thank Prof. Andrew M. Weiner for providing me with the research opportunities; for his efficient guidance, insightful discussions, and consistent encouragement; and for his great patience watching me taking baby steps.

Thank my committee members, Prof. Kevin J. Webb, Prof. Mark R. Bell and Prof. Minghao Qi, for taking their precious time to consider my work.

Thank Dr. Daniel E. Leaird for his numerous technical support and invaluable discussions and help. Without him, the experiments would be much more painful and time inefficient.

Thank previous group members Mehmet Akbulut, Shawn X. Wang, Houxun Miao and Robin Huang for their help and educational discussions. Thank Supradeepa Venkata, Ehsan Hamidi, Fahmida Ferdous, Hao Shen, Rui Wu, and Dr. Chris Long for their help and friendship. Thank Albert Vega for fixing and maintaining the mode-locked laser, which is very important for my research.

Thank everyone at Purdue University and the great Lafayette area who has ever helped me and made life more joyful.

Finally yet importantly, thank my husband Zhi Jiang for all his love, support and encouragement.

TABLE OF CONTENTS

Page

Page

LIST OF TABLES

LIST OF FIGURES

Figure Page

Figure Page

Figure Page

Figure Page

LIST OF ABBREVIATIONS

ASE	Amplified Spontaneous Emission
BER	Bit Error Rate
CCD	Charge Coupled Device
CSRZ	Carrier-Suppressed Return-to-Zero
DEMUX	Demultiplexer
DGD	Differential Group Delay
DPSK	Differential Phase Shift keying
DUT	Device Under Test
DWDM	Dense Wavelength Division Multiplexing
EDFA	Erbium Doped Fiber Amplifier
FLC	Ferroelectric Liquid-Crystal
FWHM	Full Width at Half Maximum
HWP	Half Wave Plate
ITU	International Telecommunication Union
LHC	Left-Hand Circular
LCM	Liquid Crystal Modulator
MMM	Müller Matrix Method
MUX	Multiplexer

OOK	On/Off keying
OSA	Optical Spectrum Analyzer
OTDM	Optical Time Division Multiplexing
PBS	Polarization Beam Splitter
PC	Polarization Controller
PDL	Polarization Dependent Loss
PMD	Polarization Mode Dispersion
PSP	Principal State of Polarization
PMF	Polarization Maintaining Fiber
QWP	Quarter Wave Plate
RHC	Right-Hand Circular
rms	Root Mean Square
RZ	Return-to-zero
SMF	Single Mode Fiber
SOP	State of Polarization
VIPA	Virtual Imaged Phased Array
WDM	Wavelength Division Multiplexing

ABSTRACT

Xu, Li. Ph.D., Purdue University, May 2010. All-Order Polarization Mode Dispersion Sensing and Compensation in Optical Fiber Communication Systems.
Major Professor: Andrew M. Weiner.

Polarization Mode Dispersion (PMD) is considered a major obstacle for ultrahigh-capacity fiber communication systems at 40 Gbaud/s and above. It arises from the residual birefringence of the optical fiber, and causes a differential group delay between different polarizations. If the delay is comparable to a significant fraction of the bit period, adjacent bits may overlap, leading to an increase in bit error rate. Moreover, for polarization multiplexing (Pol-Mux) used in ultrahigh-capacity fiber systems as an important method to improve spectral efficiency, PMD not only couples polarization-multiplexed channels, but also lowers transmission tolerance to fiber nonlinearity and chromatic dispersion. Therefore, for fiber spans in which the PMD is not very small, PMD compensation (PMDC) is required.

PMD monitoring is an essential part of PMDC. Since PMD can occasionally vary on a millisecond scale, and the frequency dependence of the PMD becomes important, a fast frequency-resolved monitoring tool is preferred. We experimentally apply a unique high-speed spectral polarimeter to realize near-real-time broadband Polarization Mode Dispersion (PMD) measurements.

Based on PMD sensing work, our group has previously performed all-order PMD compensation via hyperfine resolution optical pulse shaping for isolated short pulses. This scheme works more efficiently than the traditional compensators that are limited to the low-order PMD regime and valid only for small distortion compared with pulse width. Here for the first time, we apply this technique in optical fiber communication system experiments: (1) 40 Gbit/s systems; (2) 10 Gbit/s×2 Pol-Mux systems. For the 40 Gbit/s system, we construct a test-bed realized by 10 Gbit/s × 4 optical time division multiplexing (OTDM). With this system, employing an optical pulse shaper with 128

pixels to control 200 GHz range, we demonstrate all-order PMDC with over 50 ps mean differential group delay. For the 10 Gbit/s × 2 Pol-Mux (10% RZ) system, with the same shaper we compensate PMD with over 40 ps mean differential group delay. Both experiments can readily be extended to higher symbol rate (pulses down to sub-ps range).

1. INTRODUCTION

Optical fiber communication systems enable the explosive development of internet technique and the information exchange among personal computers, due to its high capacity and fast speed in long-haul signal transmission. As shown in figure 1.1, the information traffic has grown significantly for the past several years, and this trend is still going on solidly. This growth requires increasingly higher capacity of dense wavelength division multiplexing (DWDM, 50 GHz channel spacing), as shown in figure 1.2. DWDM of 100 Gbit/s capacity is needed by the year 2010 [1]. Requirement for even higher capacity is on the way. To realize this high capacity, large symbol rate (10 G/s, or even 20 G/s, 40 G/s) together with multi-level modulation format is used.

However, polarization mode dispersion (PMD) in optical fiber has become a major limitation for these high-capacity optical communication systems. PMD is caused by the randomly varying birefringence in optical fiber, and it varies occasionally on a millisecond scale [2]. To the first order approximation, PMD is described by differential group delay (DGD) between two principal states of polarizations (PSP) [3]. DGD broadens and distorts optical signal, causing system penalty. It is a random variable with Maxwellian probability function [3], and mean value is proportional to square root of fiber length due to the random polarization coupling. Usually the mean DGD less than 10% of the bit period is allowed without any significant penalty by the International Telecommunication Union (ITU) guidelines. As a result, PMD limits the transmission length, as shown in figure 1.3. Many existing fibers are early installed and have up to $0.4 ps/\sqrt{km}$ PMD, and the transmission reach of 40G/s symbol rate is less than 50 km. To reduce PMD effect, the simplest way is to deploy low PMD fibers, though the cost is large. For newly installed state-of-art low PMD fibers with only $0.05 ps/\sqrt{km}$ PMD, it allows 40 G/s symbol rate to transmit 2500 km (may be still less than transoceanic distance). However, erbium doped fiber amplifiers (EDFA) also introduce PMD with typical value of 1 ps each [4], and this reduces the above 2500 km transmission reach to only 480 km, as shown in figure 1.4. To achieve high capacity in

long transmission reach, PMD compensation has become required for today and the future.

PMD monitoring is an essential part of PMD compensation. There exist several established PMD measurement methods. Some of them give partial information of PMD, for example, degree of polarization (DOP) measurement, and fixed analyzer method [5] to measure mean DGD. Others can fully describe PMD by obtaining PMD vector as a function of frequency, like Jones matrix eigenanalysis (JME) method [6] and Muller matrix method (MMM) [7], and Poincare arc analysis method [8, 9]. Moreover, PMD can occasionally vary on a millisecond scale, so a fast frequency-resolved monitoring tool is preferred. We experimentally apply a unique high-speed spectral polarimeter [10] to realize near-real-time broadband Polarization Mode Dispersion (PMD) measurements [11]. Chapter 3 shows this work in detail.

PMD compensation can be performed in both electrical and optical domain. In electrical domain, there are several kinds. The first kind is to use diversity receivers [4] to detect optical signal in two or more polarization states to allow DGD or even principal state of polarization (PSP) information to be estimated, and then apply time delay between the right polarization states to perform first-order correction. The second kind is electrical equalization, including several different methods: (1) transversal filter (adaptively change the receiver filter shape to compensate certain PMD distortion). (2) decision feedback (dynamically adjust decision threshold). (3) maximum likelihood detection (collect several bit periods to statistically process and estimate the most probable bit pattern). Recently, a technique contained both phase and polarization diversity detection and complicated equalization circuit with digital data processing is developed to compensate PMD for Dual-Polarization QPSK signal [12]. Using this technique, AT&T lab demonstrated a transceiver in 2008, which realize real-time all-order PMD compensation of over 50-ps mean DGD in electrical domain for 46 Gbps (11.5 G/s symbol rate) Dual-Polarization QPSK signal [13]. The advantage of electrical compensation is that it can be implemented on integrated circuits. However, it is very complex to design. It is also expensive for high symbol rate (>10 G/s). To date, experiments reaching to 40 Gbaud/s are limited.

Optical domain PMD compensation is another option. The schemes of other groups are concluded in two kinds: PMD compensation at the transmitter and at the receiver. For the first kind (PMD compensation at transmitter), input SOP is aligned to one of the PSP of the system [14] so that PMD does not affect transmission. A polarization controller is used to realize the alignment with the help of a feedback loop

from the receiver, as shown in figure 1.5. This technique only works with narrow bandwidth. The transmission of the feedback signal is also challenging. For the other kind (PMD compensation at the receiver), an opposite PMD is added to null PMD vector of the system. For the simplest type, a fixed or tunable differential delay element is used [15]. A feedback loop controlled polarization controller is used to align the PMD vector of the compensator, as shown in figure 1.6. This compensates first-order PMD, and thus operates in narrow bandwidth. Some other work use two or more stages of fixed or tunable differential delay element in order to handle second-order PMD as well. More parameters need to be tuned based on feedback loop, and local optimization becomes a problem. As stages increase, design becomes more complicated.

Previously our group demonstrates all-order PMD compensation in optical domain at receiver. In one work, PMD compensation is performed [16] in a virtually imaged phased-array-based transmission pulse shaper. All-order PMD distorted pulse is recovered from 100ps width to original 15 ps. This scheme works more efficiently compared with the traditional optical PMD compensators that typically work in the low-order PMD approximation. As shown in figure 1.7, the optical signal spectrum is dispersed by a 200 GHz virtually imaged phased array (VIPA) [17] to free space, and frequency resolved PMD is monitored by a polarimeter and then compensated by liquid crystal modulator (LCM) arrays. In the other work, PMD compensation is performed [18] in a grating based transmission pulse shaper, in which 800 fs pulses were fully compensated after being distorted to >10 ps by all-order PMD. However, in these work the compensator was tested with low repetition rate (50 MHz), isolated pulses. Now for the first time, we apply this technique in optical fiber communication experiments: (1) 40 Gbit/s system; (2) 10 Gbit/s×2 Pol-Mux system.

For the 40 Gbit/s system, we construct a test-bed realized by 10 Gbit/s × 4 optical time division multiplexing (OTDM). We choose 10 Gbit/s ×4 OTDM signal, because its polarization mode dispersion property is equal to 40 Gbaud/s symbol rate signal, while it can be generated and detected by our 10G instruments. For this test bed, efforts are taken to realize modules such as the appropriate optical source, 10G-to-40G multiplexing, 40G-to-10G demultiplexing, and special modulation (to make PMD sensing on 10 Gbit/s ×4 OTDM possible). With this system, employing an optical pulse shaper with 128 pixels to control 200 GHz range, we report compensation for PMD with mean differential group delay of more than 50 ps, twice the symbol period and well into the all-order regime. The details are show in chapter 4.

We also apply our PMD compensation technique in a 10 Gbit/s×2 Pol-Mux system. The motivation is that polarization multiplexing (Pol-Mux) becomes popular in ultrahigh-capacity fiber systems as an important method to improve spectral efficiency. However, Pol-Mux signal is even vulnerable to PMD effect, because PMD not only distorts and broadens the pulse but also couples polarization-multiplexed channels. Moreover, PMD lowers its transmission tolerance to fiber nonlinearity and chromatic dispersions [19]. For fiber span with not small PMD, PMD compensation technique is required to make Pol-Mux transmission feasible. We construct a test bed for PMD compensation in a 10 Gbit/s×2 Pol-Mux RZ (10%) system. With the same shaper, we compensate all-order PMD with over 40 ps mean differential group delay. The details are shown in chapter 5.

Currently in these two PMD compensation experiments, our results show the ability of compensating PMD distortion effects so large that they are usually viewed as intractable. In the future, these experiments can readily be extended to higher symbol rate (pulses down to sub-ps range) where strong PMD effects are increasingly likely to occur, since our pulse shaping approach has been demonstrated to scale to pulses in the sub-picosecond regime [18]. The summary of our work and the future directions are given in chapter 6.

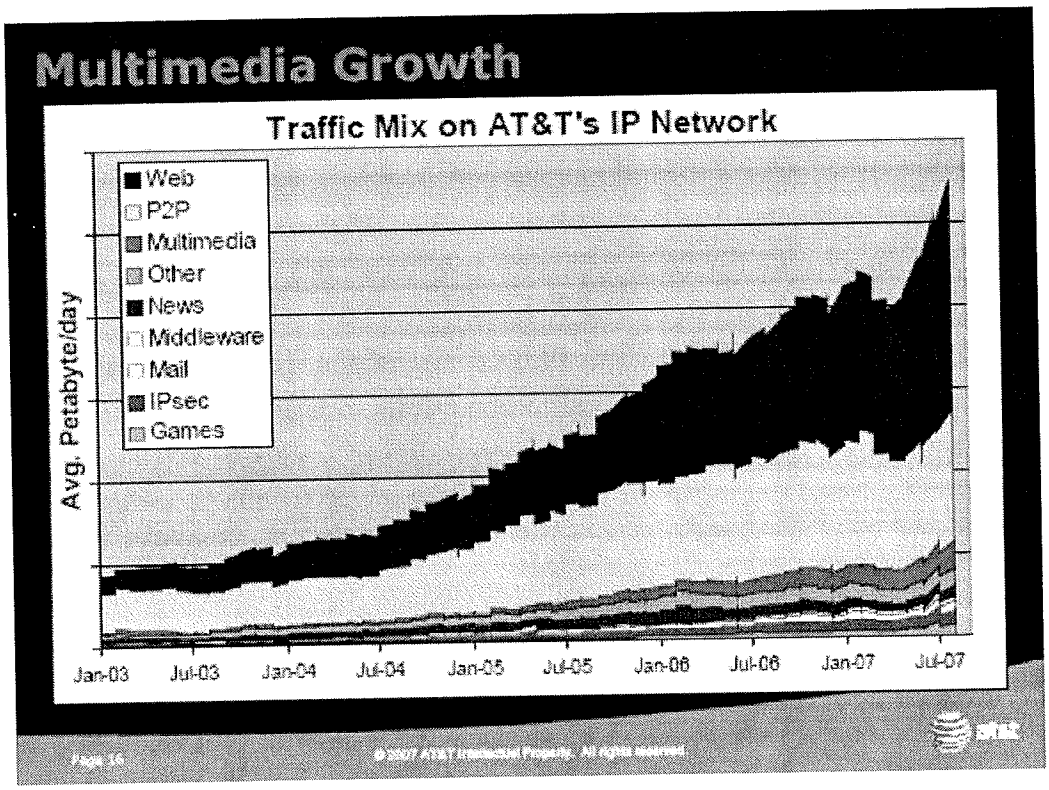

Fig. 1.1 Multimedia growth from Jan-03 to Jul-07. (Adapted from [1])

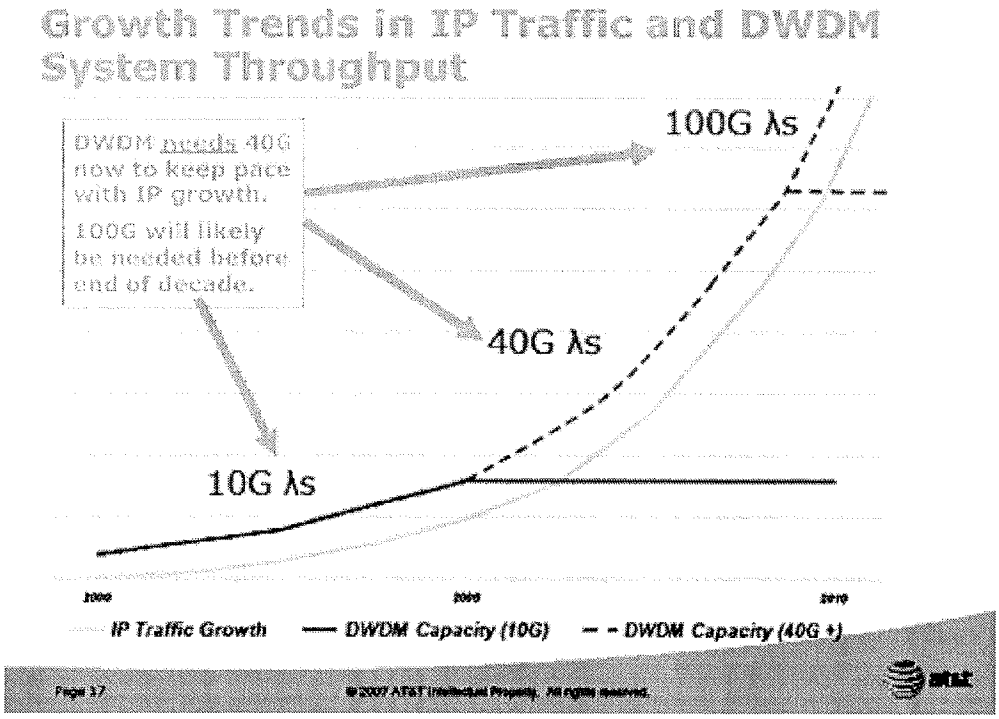

Fig. 1.2 The IP Traffic growth and DWDM capacity growth trend needed. (Adapted from [1])

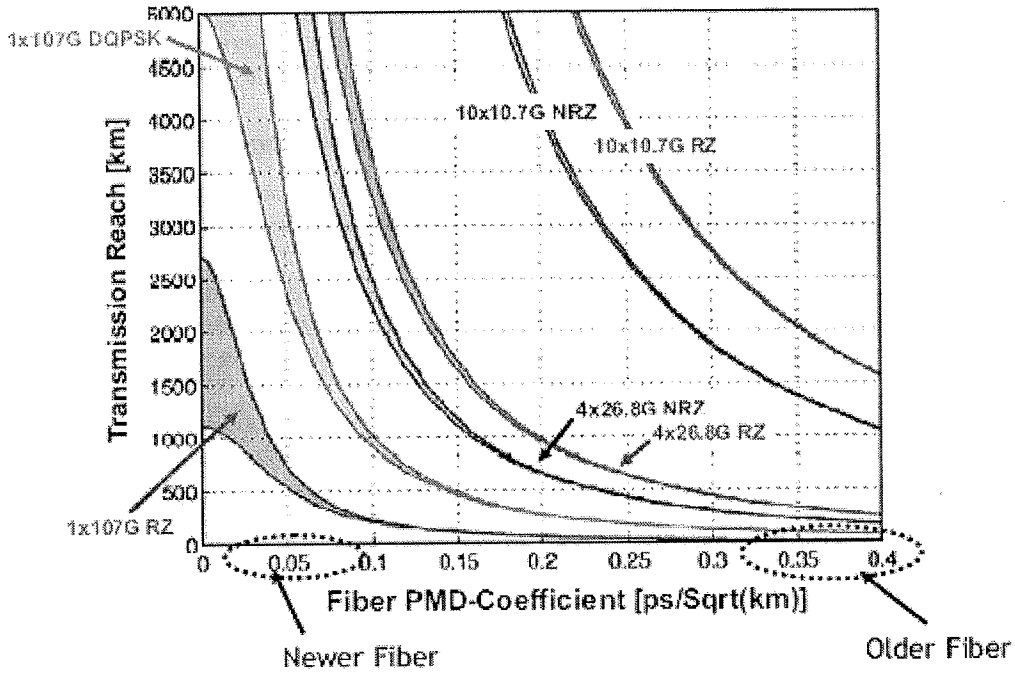

Fig. 1.3 Transmission reach vs. fiber PMD-coefficient. (Adapted from [1])

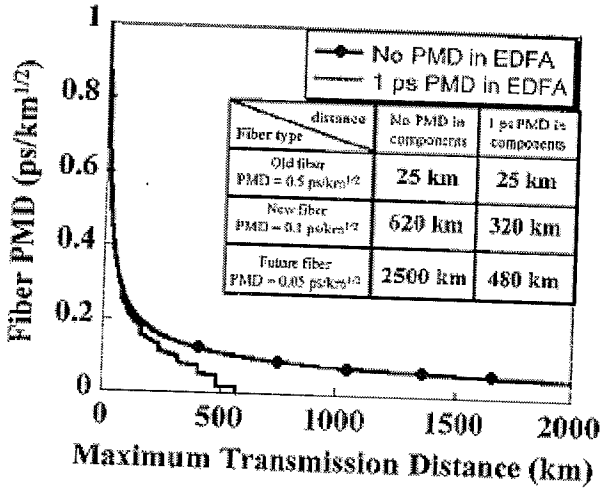

Fig. 1.4 Fiber PMD vs. transmission distance for 40 Gbit/s, 90-km EDFA spacing. (Adapted from [4])

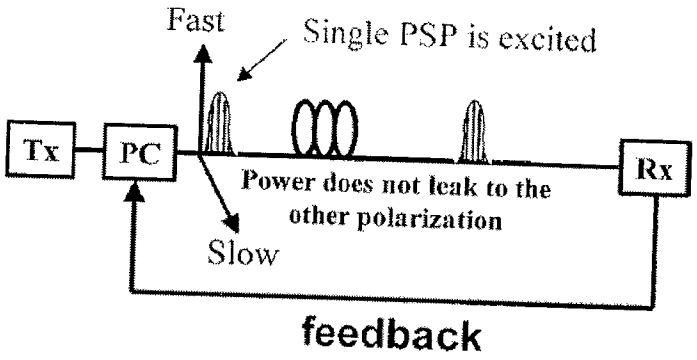

Fig. 1.5 PMD compensation at transmitter (adapted from [4]).

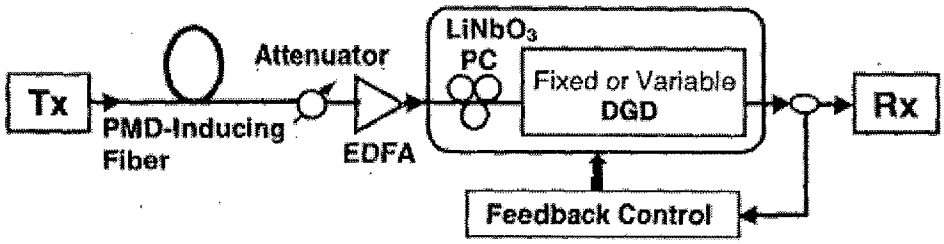

Fig. 1.6 First order PMD compensation using a differential delay element at receiver (adapted from [15]).

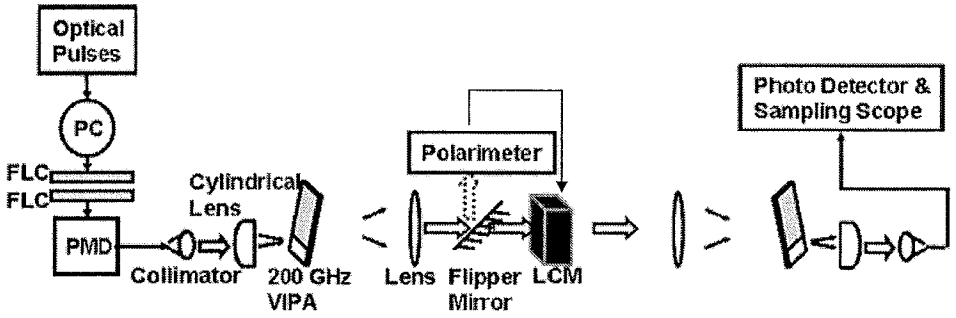

Fig. 1.7 All-order PMD compensation using liquid crystal modulator array. (adapted from [16])

2. PMD FUNDAMENTALS

The PMD basics are introduced in this chapter, including polarization states of light beam, the two origins of PMD in optical fiber (birefringence and polarization mode coupling), the concept of principal state of polarization, and the PMD vector.

The polarization state is an important parameter of light beams. A device can change this parameter. People use two different methods to describe the polarization state and the effect of a device in changing polarizations: Jones calculus (Jones vector and Jones matrix), and Stokes space (Stokes vector and Müller matrix) [20]. The details are shown in section 2.1. In optical fiber, the existence of the birefringence makes the two polarizations of the light beam lose their degeneracy in propagation constant, and thus cause the differential group delay (DGD) between them. Section 2.2 discusses the birefringence in optical fiber and its effect on polarization. Polarization mode coupling is another cause of polarization mode dispersion, as shown in section 2.3. This coupling together with birefringence make the PMD complicated in long fibers. However, the concept of principal state of polarization describes the PMD in a simple way. This important concept is introduced in section 2.4. People use PMD vector as a function of frequency to fully describe PMD. Section 2.5 discusses the properties of the PMD vector.

2.1 Polarization of Light Beam

As the light beam propagates in the z direction, the electric field, which lies in the x-y plane, can be viewed as the superposition of two orthogonal linearly polarized fields: x and y components. In time domain, for any point in space, the electric field is [20]:

$$\vec{\varepsilon}(t) = \vec{a}_x E_{x0} \cos(\omega t + \phi_x) + \vec{a}_y E_{y0} \cos(\omega t + \phi_y) \tag{2.1}$$

In the above equation, E_{x0} and E_{y0} are the amplitudes of the x and y component respectively, while ϕ_x and ϕ_y are the phase of these two components. We can see that the electric field varies with time, but the variations are different due to the difference in amplitudes and phases of the components. We use State of

Polarization (SOP) to name this variation. In the case $\phi_x = \phi_y$, the field direction, which is determined by the ratio of E_{x0} and E_{y0}, is constant, and we get linear polarization. In the case $\phi_x \neq \phi_y$, we get elliptical polarization, which means that the end of the electric field vector evolves on an ellipse in the x-y plane with time. If $\phi_x > \phi_y$, the ellipse is left-handed, which means the evolution is counter-clockwise, while if $\phi_x < \phi_y$, the ellipse is right-handed, which means the evolution is clockwise. (We always assume that the observer looks towards the propagation direction of the light.) Table 2.1 summarizes the SOPs in different cases.

Jones calculus is a simple and clear way to describe SOP and the media where the light propagate and its SOP evolves. Jones claculus includes 2×1 Jones vectors which describe the SOP, and 2×2 Jones matrices which describe the media. In Jones calculus, the electric field of a certain SOP is written as:

$$E = \begin{bmatrix} E_x \\ E_y \end{bmatrix} = \begin{bmatrix} E_{x0}e^{j\phi_x} \\ E_{y0}e^{j\phi_y} \end{bmatrix} \tag{2.2}$$

If we normalize the Jones vector, all the SOP can be written as:

$$\begin{bmatrix} \cos\theta \\ \sin\theta \times e^{j(\phi_y-\phi_x)} \end{bmatrix} \tag{2.3}$$

The normalized Jones vector for horizontaly and vertically linear polarization and the right-hand and left-hand circular polarization are:

$$\begin{bmatrix} 1 \\ 0 \end{bmatrix}, \begin{bmatrix} 0 \\ 1 \end{bmatrix}, \frac{1}{\sqrt{2}}\begin{bmatrix} 1 \\ j \end{bmatrix}, \frac{1}{\sqrt{2}}\begin{bmatrix} 1 \\ -j \end{bmatrix} \tag{2.4}$$

If the two SOPs E_1 and E_2 are orthogonal, this means these two Jones vector satisfies: $Dot(E_1, E_2^*) = 0$, where E_2^* is the conjugate of E_2. Obviously, Horizontal linear polarization and vertical linear polarization, RHC and LHC are two orthogonal pairs. Any SOP can be decomposed to the combination of two orthogonal SOP pairs.

When the light propagate in a media, its SOP evolves. We use Jones matrix to describe how this media changes the input SOP into the output SOP. The relationship is :

$$\begin{bmatrix} E_{xout} \\ E_{yout} \end{bmatrix} = \begin{bmatrix} J_{11} & J_{12} \\ J_{21} & J_{22} \end{bmatrix} \begin{bmatrix} E_{xin} \\ E_{xout} \end{bmatrix} \tag{2.5}$$

where $J = \begin{bmatrix} J_{11} & J_{12} \\ J_{21} & J_{22} \end{bmatrix}$ is Jones Matrix. For example, here we introduce two simple but frequently used Jones matrix. One is for the retarder (or waveplate) with its fast axis at x axis:

$$R(\phi)=\begin{bmatrix} e^{j\frac{\phi}{2}} & 0 \\ 0 & e^{-j\frac{\phi}{2}} \end{bmatrix} \tag{2.6}$$

it retards the phase of y field component by ϕ. The other one is for rotating the x-y coordinates by angle θ relative to the +x axis:

$$S(\theta)=\begin{bmatrix} \cos\theta & \sin\theta \\ -\sin\theta & \cos\theta \end{bmatrix} \tag{2.7}$$

For a complicated or composite optical device, to get its Jones matrix, we multiply the Jones matrix of the simple operations or the individual elements in order. In a system with no loss, the Jones matrix can be simply expressed as the products of the Jones matrixes for retarders and axis rotations.

Similar to Jones calculus, Stokes vector and Müller matrix in Stokes space is another way to describe SOP and the media. Stokes parameters (s_0, s_1, s_2, s_3) are measurable parameters [21,22]:

$$\begin{aligned} s_0 &= I_0 + I_{90} = I_{45} + I_{135} = I_{RHC} + I_{LHC} = E_{x0}^2 + E_{y0}^2 \\ s_1 &= I_0 - I_{90} = E_{x0}^2 - E_{y0}^2 \\ s_2 &= I_{45} - I_{135} = 2E_{x0}E_{y0}\cos(\phi_y - \phi_x) \\ s_3 &= I_{RHC} - I_{LHC} = 2E_{x0}E_{y0}\sin(\phi_y - \phi_x) \end{aligned} \tag{2.8}$$

where I_0 is the intensity of the horizontal component, and the meaning of I_{90}, I_{45}, I_{135}, I_{RHC} and I_{LHC} are similar. The Stokes vector is the normalization of the vector (s_1, s_2, s_3). This vector is always plotted on the unit sphere known as Poincarè sphere in 3-D space. By this tool, SOP can be visualized and conveniently analyzed. Figure 2.1 shows the SOPs denoted by different points on Poincarè sphere. In this figure, the $+s_3$ axis points downward, but in the rest part of this thesis, we choose this axis upward. Table 2.2 shows the Stokes vetor for some special SOPs.

On the Poincarè sphere, all the linear polarizations lie on the equator. The north pole and the south pole are LHC and RHC respectively. SOPs are left-hand elliptical on the north of the sphere, and right-hand elliptical on the south. Every pair of orthogonal SOPs are the two points symmetric about the center of the sphere.

In Stokes space, a 3×3 matrix called Müller matrix describe the media's effect on the SOP evolution.

Jones calculus and the Stokes vector have their own advantage comparing with each other. Jones vector and matrix are smaller in size, and they describe the field directly. However, Jones vector can only describe polarized light, while Stokes vector

can also describe partially polarized light and unpolarized light. Moreover, visualization is also an advantage of Stokes space.

2.2 Birefringence in Optical Fibers

In optical fiber communication systems, although we call the optical fiber as single mode fiber (SMF), there exist two orthogonally polarized HE11 modes [3,23]. If the fiber has not only perfectly symmetric core and cladding geometry but also perfectly isotropic material (as shown in Figure 2.2 (a)), these two modes have the same group delay. However, in the real world, the symmetry of the fibers is destroyed according to the internal perturbation and/or the external perturbation. So that the degeneracy of the two orthogonally polarized modes is broken: birefringence exists, or in the other words, the phase and group velocities of the two modes are different.

The internal perturbation comes from the manufacturing process and has two kinds [24]. One kind is that the core is elliptical (as shown in Figure 2.2 (b)). In this case, geometric birefringence arises and the two HE11 modes have different propagation constants. The other kind is that though the core is circular, there exist asymmetric internal stress (as shown in Figure 2.2 (c)), which causes the material density difference, and thus the difference of the propagation constant of the two modes.

The external perturbation [3,24] (as shown in Figure 2.2 (c)) includes lateral stress, bending, and twist. The first two have the similar effects as the internal asymmetric stress, so they cause linear birefringence by introducing material density difference. Unlike all the other perturbation, fiber twist creates circular birefringence. We only discuss linear birefringence in this thesis.

The birefringence of single mode fibers is on the order of $10^{-5} \sim 10^{-7}$ [3,24], which is small compared with the refractive index of the core (~1.5), but in the long communication optical fiber it can cause large differential group delay between fast mode and slow mode compared with the pulse width of optical signal. The perturbation on single mode fiber is randomly distributed along the length. Ideally, in a short section of single mode fiber, the birefringence can be considered uniform. In this case, it can be viewed as a wave plate. The slow mode and the fast mode have difference in the propagation constant:

$$\Delta\beta = \beta_{slow} - \beta_{fast} = \frac{\omega n_{slow}}{c} - \frac{\omega n_{fast}}{c} = \frac{\omega \Delta n}{c} \tag{2.9}$$

Where c is the speed of light, ω is the angular frequency of light, and n_{slow} and n_{fast} are the effective refractive index of the slow mode and the fast mode respectively. If the input wave is linearly polarized along the birefringence axis, only one mode is excited, and the SOP is maintained along the length of the fiber. Otherwise, both of the fast and slow modes are excited, and the input SOP is decomposed to the two modes which are orthogonal. Figure 2.3 (a) illustrates how an arbitrary SOP is decomposed to a pair of orthogonal SOPs on Poincarè sphere (Stokes space). Point A and point B denote the two orthogonal modes SOP1 and SOP2 on Poincarè sphere, and they are symmetric about the sphere center. Point C denotes an arbitrary SOP3. If we project C on the section AB, and cut it into two sections with length l_1 and l_2. We get the relation:

$$E_3 = a_1 e^{j\phi_1} E_1 + a_2 e^{j\phi_2} E_2 \tag{2.10}$$

and

$$\frac{a_1^2}{a_2^2} = \frac{l_2}{l_1} \tag{2.11}$$

In equation 2.10, the Jones vector of SOP3 is written as the combination of this orthogonal pair. The intensity ratio of each components is determined by the ratio of l_1 and l_2. With fixed intensity ratio, if the phase difference of the two components changes, SOP3 evolves on a circle. Figure 2.3 (b) gives an example of such evolution. An arbitrary SOP is decomposed to two orthogonal modes (fast mode and slow mode). As it propagate along the fiber, and the phase difference between two modes increases while the intensity ratio remains the same. The SOP evolves on the circle with line AB as its axis and returns to its original SOP after propagating a fiber length named 'Beat Length' [3].

The beat length is:

$$L_B = \frac{2\pi}{\beta_{slow} - \beta_{fast}} = \frac{2\pi}{\omega \Delta n / c} = \frac{\lambda}{\Delta n} \tag{2.12}$$

For 1550nm wavelength and $\Delta n \sim 10^{-7}$, the beat length is $\sim 15m$, and for polarization maintaining fiber (PMF) with $\Delta n \sim 4 \times 10^{-4}$, the beat length is about 3mm.

If the input SOP is fixed, but the light contains different frequency components, then for an ideal short fiber (which means the birefringence is uniform along its length) with fixed length the output SOP vs. frequency evolves in a similar way on Poincarè sphere. In the case that only one mode is excited, then the output SOP from this ideal short birefringence maintains the same with the input SOP for all frequencies. If two

modes are excited, the output SOP vs. frequency traces the circle on the Poincarè sphere surface. The circle also has line AB as its axis.

For this fixed length ideal short fiber, considering two modes in time domain, there is differential group delay (DGD) $\Delta\tau$ between them. The DGD is proportional to the fiber length. This polarization mode dispersion (PMD) is usually characterized as:

$$\frac{\Delta\tau}{L} = \frac{d\beta_{slow}}{d\omega} - \frac{d\beta_{fast}}{d\omega} = \frac{d}{d\omega}\left(\frac{\Delta n\omega}{c}\right) = \frac{\Delta n}{c} + \frac{\omega}{c}\frac{d\Delta n}{d\omega} \tag{2.13}$$

The first term is independent of frequency. The second term is the dispersion of Δn, which is small compared with the first term. In this thesis, we ignore the second term in our simulation and calculation.

2.3 Polarization Mode Coupling

In the short length of single mode fiber, where the perturbation is considered uniform, the DGD is deterministic. However, in the long-haul optical fiber communication systems, the perturbation on fiber is random. Not only the scale of the birefringence is not uniform, but also the axes of the birefringence are random. These random axes cause polarization mode coupling. The slow and fast polarization modes from one segment are both decomposed to the slow and fast mode in the next segment. People use the concatenation of wave plates with random oriented birefringence axes to model long fiber [3], as shown in figure 2.4.

In such a long fiber, DGD does not accumulate linearly with fiber length. The perturbation on fiber can be affected by the environment temperature and the stress imposed, so the DGD changes randomly along fiber length with time due to these factors. Statistics is usually used to analyze PMD in long fiber. It shows that the average DGD of a long fiber is proportional to the square root of the fiber length [25].

2.4 Principal State of Polarization

In time domain, when pulse propagates along a long fiber, it has random mode coupling as the birefringence axes changes. The pulse splits at every axis change and thus become complicated. In frequency domain, the output SOP for different frequencies traces an irregular trajectory on Poincarè sphere. In 1986, Poole and

Wagner developed the Principal States Model for long fibers [26]. It characterizes PMD both in time domain and frequency domain. In time domain, when people launch the signal of different SOPs into the long fiber which has PMD much smaller than the pulse width and has no polarization dependent loss (PDL), there exist two orthogonal launch SOP so that the bit-error rate are minimum. In these two cases, the pulses are undistorted, and they are the slowest and the fasted pulses of the entire different SOPs launched. These two SOPs are called principal state of polarization (PSP). In frequency domain, input PSP is defined as the input SOP such that the output SOP is independent of frequency over a small span to the first order. The corresponding output SOP is called output PSP. Without PDL in systems, the input PSPs and output PSPs are two orthogonal pairs. The output PSP is related to the input PSP by the transmission matrix of the fiber. In Jones calculus, the relation is:

$$E_{out}(\omega) = JE_{in}(\omega) \tag{2.14}$$

In Stokes space, the relation is:

$$S_{out}(\omega) = R(\omega)S_{in}(\omega) \tag{2.15}$$

For ideal short fibers, the PSPs are the birefringence axes, as shown in Figure 2.5(a). The output PSP is the same for all the frequency. For a fixed input SOP, the output SOPs for different frequencies are on a circle that is symmetric about the birefringent axis. Though for long fibers, with a fixed input SOP the output SOP for different frequencies traces an irregular trajectory rather than a circular on Poincarè sphere, but within a small frequency span centered at certain frequency, the SOP is approximately on an arc which is a part of the circle symmetric about the PSP for this certain frequency. As shown in Figure 2.5(b), for a certain frequency ω_1 and a small span $\Delta\omega$, $SOP(\omega_1 - \Delta\omega/2)$ and $SOP(\omega_1 + \Delta\omega/2)$ are approximately on the circle symmetric about $PSP(\omega_1)$. Assume that the angle of the arc between $SOP(\omega_1 - \Delta\omega/2)$ and $SOP(\omega_1 + \Delta\omega/2)$ is $d\varphi$, then the DGD between the two orthogonal PSPs of frequency ω_1 is:

$$\tau(\omega) = \left|\frac{d\varphi}{d\omega}\right| \tag{2.16}$$

2.5 PMD Vector

In Principal States Model, PSP and DGD are the two key parameters to characterize PMD. We use PMD vector $\vec{\tau}$ to combine these two parameters together [3]. This vector is a vector in Stokes space. Its direction is the slower PSP, and its

magnitude is the DGD between the two PSPs. That is $\vec{\tau} = \Delta\tau\hat{p}$, where $\Delta\tau$ is DGD and $\hat{p}$ is slower PSP. Correspondingly, the other PSP, the faster one, is $-\hat{p}$. If we choose the output PSP, then we get the output PMD vector; and if we choose input PSP, we get the input PMD vector. They are related by:

$$\vec{\tau}_{out} = R\vec{\tau}_{in} \tag{2.17}$$

where R is the transmission matrix of the media.

PMD vector also has mathematical definition. Equation 2.15 gives the relation between the input SOP and the output SOP. If the input SOP is fixed for different frequencies, after differentiate both side of this equation, we get [3]:

$$\frac{dS_{out}(\omega)}{d\omega} = \frac{dR(\omega)}{d\omega}S_{in} \tag{2.18}$$

Using Equation 2.15, we can replace the input SOP and get:

$$\frac{dS_{out}(\omega)}{d\omega} = \frac{dR(\omega)}{d\omega}R^{-1}(\omega)S_{out}(\omega) \tag{2.19}$$

In the Equation 2.19, $\frac{dR(\omega)}{d\omega}R^{-1}(\omega)$ can be replaced by $\vec{\tau}(\omega)\times$, and we get [3]:

$$\frac{dS_{out}(\omega)}{d\omega} = \vec{\tau}(\omega)\times S_{out}(\omega) \tag{2.20}$$

Where $\vec{\tau}(\omega)$ is the PMD vector at frequency ω. This equation gives the mathematical definition of PMD vector. The PMD vector describes how the output SOP precesses around the PSP as the frequency varies given the fixed input SOP. The relative direction of $S_{out}(\omega)$ and $\vec{\tau}(\omega)$ determine the local radius of the trajectory, and the magnitude of PMD vector, or the DGD $\Delta\tau$ between two PSPs determine the rate of the precessing of $S_{out}(\omega)$ around $\vec{\tau}(\omega)$. The relation is:

$$\varphi = \Delta\tau\Delta\omega \tag{2.21}$$

where φ is the rotation angle. If the $S_{out}(\omega)$ is aligned with $\vec{\tau}(\omega)$ or $-\vec{\tau}(\omega)$, then $\frac{dS_{out}(\omega)}{d\omega} = 0$, and the output SOP is frequency independent.

PMD vector is a function of optical angular frequency. If we apply Taylor-series expansion on PMD vector around the carrier frequency ω_0 with span $\Delta\omega$, we get [27]:

$$\vec{\tau}(\omega) = \vec{\tau}(\omega_0) + \frac{d\vec{\tau}(\omega_0)}{d\omega}\Delta\omega + \ldots \tag{2.22}$$

We call the first term as the first order PMD, the second term the second order PMD, and etc. If the bandwidth $\Delta\omega$ is small enough so that the second order and higher order

PMD can be ignored, then the PMD vector is considered constant in this range. We call this bandwidth as PMD vector bandwidth, $\Delta\omega_{psp}$, which is estimated as [3]:

$$\Delta\omega_{psp} = \frac{\pi}{4}\frac{1}{\langle\Delta\tau\rangle} \tag{2.23}$$

Where $\langle\Delta\tau\rangle$ is the mean DGD for the fiber.

PMD vector concatenation rule is powerful to determine the total PMD vector of concatenated elements when the PMD vector for each element is known. For concatenation of two elements with output PMD vector $\vec{\tau}_1$ and $\vec{\tau}_2$ respectively, the total output PMD vector is [3, 28]:

$$\vec{\tau}(\omega) = \vec{\tau}_2(\omega) + R_2(\omega)\vec{\tau}_1(\omega) \tag{2.24}$$

Where $R_2(\omega)$ is the transmission matrix of the second element. Figure 2.6 gives a simple interpretation. Furthermore, if we apply this equation repeatedly, we can get the total PMD vector for the concatenation of more than two elements.

Similarly, there is also a concatenation rule on the input PMD vector:

$$\vec{\tau}_{in}(\omega) = \vec{\tau}_{1in}(\omega) + R_1(\omega)^{-1}\vec{\tau}_{2in}(\omega) \tag{2.25}$$

where $\vec{\tau}_{1in}(\omega)$ and $\vec{\tau}_{2in}(\omega)$ are the input PMD vectors of the first and the second element repectively, and $R_1(\omega)$ is the transmission matrix of the first element.

The relation between the output PMD vector and the input PMD vector is:

$$\vec{\tau}(\omega) = R_2(\omega)R_1(\omega)\vec{\tau}_{in}(\omega) \tag{2.26}$$

This concatenation rule can be used to design PMD emulator, or estimate the PMD of an emulator. More examples are shown in chapter 3.

Table 2.1
SOPs of different kinds

condition	$\phi_x = \phi_y$	$\phi_x > \phi_y$	$\phi_x < \phi_y$
SOP	linear polarization, $\tan\theta = \frac{E_{y0}}{E_{x0}}$, ($\theta$ is the field direction from +x axis)	Left-handed elliptical polarization.	Right-handed elliptical polarization.
		If $\phi_x = \phi_y + \frac{\pi}{2}$ and $E_{x0} = E_{y0}$, Left-hand circular (LHC)	If $\phi_y = \phi_x + \frac{\pi}{2}$ and $E_{x0} = E_{y0}$, Right-hand circular (RHC)

Table 2.2
Stokes vectors for different SOPs

(s_1, s_2, s_3)	SOP
(1, 0, 0)	Horizontal linear polarization
(−1, 0, 0)	Vertical linear polarization
(0, 1, 0)	45 degree linear polarization
(0, −1, 0)	135 degree linear polarization
(0, 0, 1)	Right-hand circular polarization
(0, 0, −1)	Left-hand circular polarization
$s_3 = 0$	Linear polarization
$s_3 < 0$	Left-hand elliptical polarization
$s_3 > 0$	Right-hand elliptical polarization

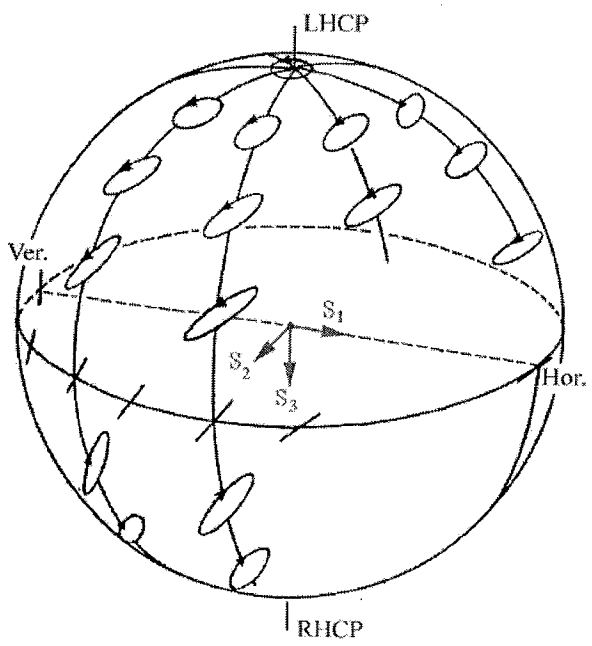

Fig. 2.1 Poincarè sphere. (Adapted from [21])

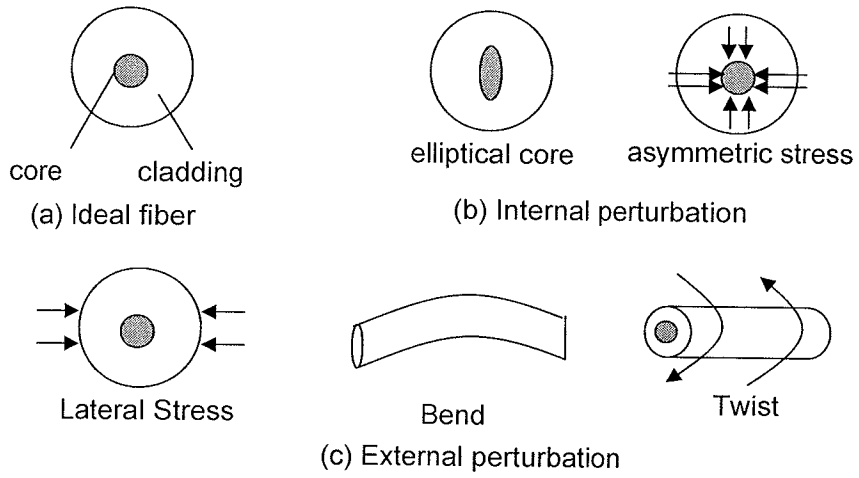

Fig. 2.2 (a) Ideal fiber (b) Internal perturbation (c) External perturbation. (Adapted from [24])

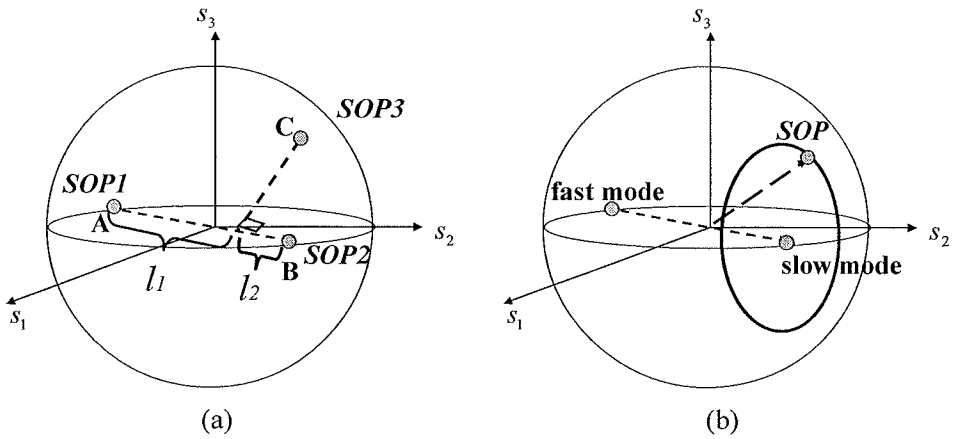

Fig. 2.3 (a) Decompose a SOP to an orthogonal SOP pair. (b)SOP on a circle on the Poincarè sphere.

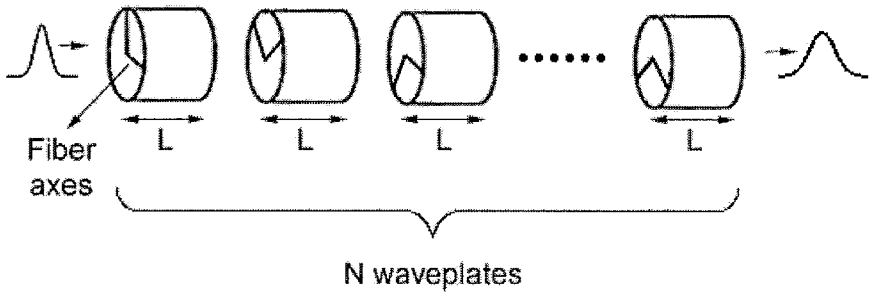

Fig. 2.4 Model long fibers by concatenation of wave plates with birefringence axes oriented randomly along the fiber length.

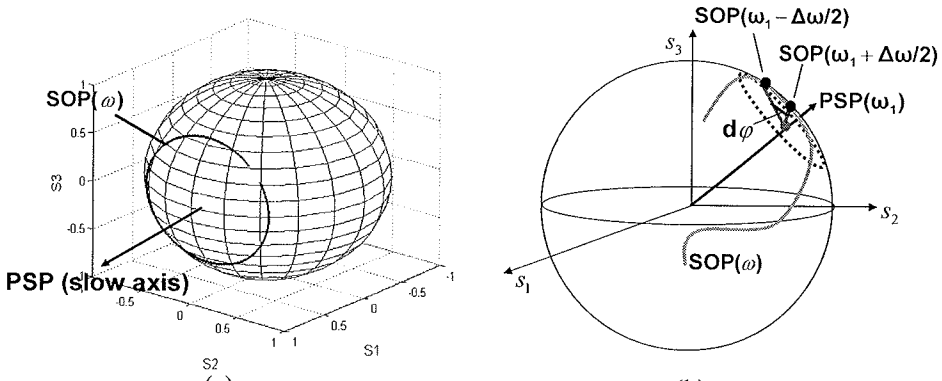

Fig. 2.5 (a) Output principal state of polarization for an ideal short fiber is the birefringent axis, and it is the same for all frequency. (b) Output PSP of a certain frequency for a long fiber.

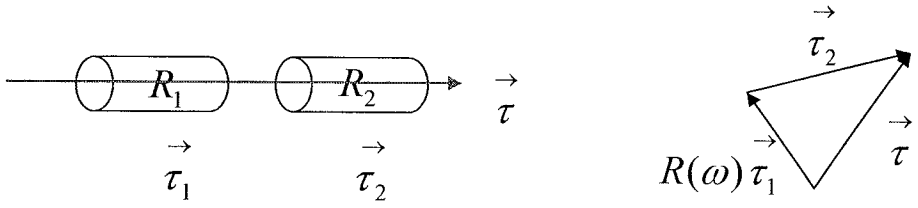

Fig. 2.6 Concatenation rule of PMD vectors

3. PMD SPECTRUM MEASUREMENT VIA HIGH SPEED WAVELENGTH-PARALLEL POLARIMETRY

Polarization mode dispersion (PMD) can be fully described by the frequency-dependent PMD vector, which specifies both the differential group delay (DGD) spectrum and the principal state of polarization (PSP) spectrum [3]. Since PMD can occasionally vary on a millisecond scale [2], fast monitoring capability for PMD is desirable. Furthermore, since the frequency dependence of the PMD vector becomes important when the DGD is large [3,29], a frequency-resolved monitoring tool is preferred.

Our laboratory has previously developed a novel wavelength-parallel polarimeter [10,30], which provides unique capabilities for high speed (millisecond time scale) characterization of frequency dependent polarization. The wavelength-parallel polarimeter has been successfully applied to monitor frequency dependent states of polarization (polarization string lengths) in a commercial 10 Gb/s WDM optical transmission systems [31]. This experiment demonstrated a tight correlation between the string length [32] and PMD-induced error rates, thereby providing evidence for polarization string length as an effective quantity for in-service PMD monitoring. The wavelength-parallel polarimeter has also been employed successfully in experiments that demonstrated the possibility of all-order PMD compensation [16,33]. In these experiments the polarimeter was used to acquire data (either the frequency dependent state of polarization [33] or the frequency dependent Jones matrix [16]) needed for control of the optical all-order PMD compensator.

In these previous reports, however, the frequency dependent PMD vector itself was not obtained. Because extracting the PMD vector requires taking frequency derivatives, it places demands that are more stringent on the quality of the polarimetry data. Now for the first time, we demonstrate extraction of the frequency dependent PMD vector by Müller Matrix Method (MMM) [7] from data acquired using the wavelength-parallel polarimeter. In order to confirm the accuracy of our results, we

perform measurements with simple PMD emulators for which characteristics of the frequency dependent PMD vector may be predicted a priori.

With this scheme, we successfully performed experiments using grating based wavelength-parallel polarimeter, which has relatively wide optical bandwidth (14 nm) and coarse spectral resolution (13.6 GHz). This is in my master thesis work [34]. Now we use virtually imaged phased array (VIPA) [17,35,36] based wavelength-parallel polarimeter, with narrower optical bandwidth (1.6 nm) but much finer spectral resolution (~3 GHz). This setup permits measurements with very large PMD, up to 90 picoseconds of mean DGD [37]. The details of this experiment are given in this chapter. In Section 3.1 we discuss the setup and the experimental procedures. Experimental results are given in Section 3.2, with a focus on extracted frequency depend PMD vectors. Finally, we conclude in section 3.3.

3.1 PMD Measurement Scheme

3.1.1 Experimental setup

Our experimental setup is as shown in Fig. 3.1 (a). 200GHz of spectrum is sliced from an ASE source and amplified by an erbium doped fiber amplifier (EDFA). A 4nm filter removes the undesired noise introduced by EDFA, and then the light goes to a polarizer. A ferroelectric liquid cell (FLC) [38] generates two SOPs separated by 90 degree in Stokes space to device under test (DUT). Then the optical spectra are dispersed by a VIPA setup in free space and measured by a linear InGaAs camera array with 128 sensing pixels. The light beam of single wavelength covers 2 sensing pixels. As a result, the resolution is ~3 GHz/pixel. The details of the VIPA setup are shown in Fig. 3.1 (b). The VIPA setup has 2.5 degree incident angle and 200 GHz free spectral range (FSR). If we use broadband light, frequency components from different FSRs overlap. For this reason, we have limited our input spectrum to 200 GHz. The frequencies dispersed by the VIPA are mapped nonlinearly [36] across the camera sensing array. This effect is carefully calibrated and corrected in software subsequent to data acquisition. As for the DUTs we use 1-section, 2-section and 3-section polarization maintaining fibers (PMF). The spliced PMF samples are put in a closed temperature controlled box, so that the output SOP and the PMD remain stable during the measurement.

3.1.2 FLC in multi-SOP generator and polarimetry

In our Multi-SOP generator and SOP measurement, the ferroelectric liquid crystal cell is a key component to perform high-speed polarization control. Fig. 3.2 shows the function of a FLC cell. It works as a quarter-wave plate with rapid-switching optic axes. The birefringence axis can be switched within 100 us between two stable states separated by 45° apart by applying opposite voltage polarities (±5 V).

By placing a FLC cell after a polarizer, it is possible to generate a pair of SOP with 90 degree on Poincarè sphere. So that we can use MMM to extract PMD vector from the measured output SOP spectra.

FLCs are also used in our spectral polarimeter [30,37] as SOP component selector. We place a fixed polarizer after two FLCs, and switch the two FLCs to four different combinations as shown in Table 3.1. With this we sequentially measure the intensity of four different SOP components, I_0, I_{90}, I_{135} and I_{RHC}, which fully determine SOP.

3.1.3 Spectral polarimetry

Besides FLC cells, the spectral polarimetry setup contains a 200 GHz VIPA as spectral disperser and a line-scan camera (with each pixel 50um wide) as a detector array, as shown in Fig. 3.1 (b). The measurement speed can be very fast. The camera can measure the power of all 128 pixels within ~50us. The switching time of the FLC cells can be as fast as 100us. One complete set of SOP measurement of 128 wavelengths requires four FLC switchings, and thus the total time can be under 1 millisecond. The measurement speed in this experiment is software limited to 20 milliseconds, however, we have demonstrated less than 1 millisecond measurement speed by using an external timing circuit for the FLC and camera triggering. Due to wavelength dependence of the FLC cells, we also perform a calibration process [30] for the polarimeter, and the SOP error after the calibration was observed to be less than 2° on Poincarè sphere.

3.1.4 PMD emulator

We use several homemade PMD emulators as our devices under test (DUT). These homemade emulators are concatenations of various lengths of polarization maintaining fibers (PMF). Each PMF section can be viewed as a retarder, with differential refractive index $\Delta n \sim 4.14\times10^{-4}$ between fast and slow axes of our fibers. We splice various numbers of PMF sections with fast axes offset by different angles to produce the PMD desired. Moreover, single mode fibers are spliced at both ends as

leads. For some of the simple (few section) PMD emulators, we were able to predict their PMD characteristics from their known construction parameters (fiber lengths and splice angles) and compare directly with measurement results. Theoretically, the PMD vectors of these DUTs can be estimated using PMD vector concatenation rule [3]. It states that for concatenation of two elements with output PMD vector $\vec{\tau}_1$ and $\vec{\tau}_2$ respectively, the total output PMD vector is

$$\vec{\tau}(\omega) = \vec{\tau}_2 + R_2(\omega)\vec{\tau}_1 \tag{3.1}$$

where $R_2(\omega)$ is the SOP rotation matrix (Müller matrix) of the second element. Furthermore, this equation can be applied repeatedly for obtaining the total PMD vector of multiple concatenated PMD elements.

However, when we estimate the PMD of this kind of emulator, we have two difficulties. First, the output lead rotates the output PSPs on the Poincarè sphere in an unknown (but approximately frequency independent) way. Second, our measurement of the lengths of PM fiber sections has error comparable to the fiber beat length [3] of ~3 millimeters; and this implies large error in estimating the SOP rotation matrix of a PMF section. As a result, it is not practical to calculate the exact PMD vector of these emulators. However, the following three special cases corresponding to few-section emulators do have certain parameters that can be accurately estimated. We illustrate these by the simulation results in Fig. 3.3.

The first (simplest) case is that of a one-section PMF. Both its DGD and PSP are frequency independent, corresponding to a fixed point on the Poincarè Sphere as in Fig. 3.3(a)-(b). DGD is estimated by

$$\Delta\tau = \Delta n \times L / c \tag{3.2}$$

where L is the PMF length.

The second case is the concatenation of two PMF sections with lengths L_1 and L_2 respectively and offset angle θ between the two fast axes. By the concatenation rules for the PMD vector, the DGD is determined to be

$$\Delta\tau = \sqrt{L_1^2 + L_2^2 + 2L_1L_2\cos 2\theta} \cdot \Delta n / c \tag{3.3}$$

which is a frequency independent constant. As for the PSP, we cannot calculate the exact value because of the rotation of the SMF leads at the output side and the inability to precisely know the SOP rotation matrix of the second PMF section. However, the PSP spectrum follow a circular trajectory on the Poincarè sphere with radius r determined by L_1/L_2 and θ:

$$r = \sin(\cos^{-1}((1 + L_1/L_2 \cdot \cos 2\theta)/\sqrt{1 + L_1^2/L_2^2 + 2L_1/L_2 \cdot \cos 2\theta})) \tag{3.4}$$

We do not know the position on the PSP circle for any specific frequency. But if we cut the length L_1 of the first PMF section from the input side without touching the second PMF or the output side SMF lead, we expect the PSP circle to remain concentric with the original PSP circle. More specifically, PSPs for a fixed optical frequency retain a fixed angular location on the concentric PSP circles. Fig. 3.3 (c)-(d) shows PMD simulation results for this case.

The third case is the concatenation of 3 sections of PMF. For the same reasons as above, the DGD and PSP for individual frequencies cannot be accurately calculated. However, the DGD spectrum is periodic, as show in Fig. 3.3 (e). The period in frequency space is determined by the length of the second PMF L_2 by:

$$\Delta\omega = 2\pi c/(\Delta n L_2) \tag{3.5}$$

The PSP trajectory, shown in Fig. 3.3 (f), is more complicated than a circle and it has no estimable parameters.

To perform estimation by the equations 3.1-3.5, we measured several parameters: fiber length L, birefringence Δn, and fast axis offset angle θ. As for fiber length L, each section has error ~1mm. It is less than 0.2% of lengths of the sections, which are all larger than 50cm. In the measurement of birefringence Δn, we input ASE source to a polarizer and then a PMF section with known length L_0, and then let the light goes to another polarizer and detected by an OSA. On the spectrum measured by OSA, we get the frequency difference $\Delta\omega_0$ between two valleys. Then birefringence Δn is calculated using the relation $\Delta n = 2\pi c/(\Delta\omega_0 L_0)$. We performed these measurements with different length of PMD sections for several times, and get $\Delta n = 4.15\times10^{-4}$ within 0.5% error. For the fast axis offset angle θ, when we splice two PMF sections, we set 45° offset on the fiber splicer. We measured several 2-section emulators for which the splicer had been programmed for 45° axis offset and then measured the PSP and DGD spectrum experimentally. By fitting our results to equations 3.3 and 3.4, we found that the actual splice angle was reproducibly 40° within 0.5° error. Now that the systematic error in splicer angle calibration is known, we used this known 40° axis offset angle for our other PMD emulators. As a result, all the estimations have good accuracy. For 1-section emulator, by equation 3.2 we have 0.2% error to estimate DGD $\Delta\tau$. For 2-section emulator, by equation 3.3 the estimated DGD $\Delta\tau$ has ~1.5% error, and by equation 3.4 the estimated r has ~1% error. For 3-section emulator, by equation (5) the estimated $\Delta\omega$ has ~0.7% error. In conclusion, the precalculated parameters for these three cases have good accuracy.

3.1.5 Müller matrix method

In MMM method [7], frequency dependant Müller Matrices are measured and PMD vectors are extracted. It requires two different linear SOPs to be launched, with one polarized at 0 degree and the other one being arbitrary except 90 degree. From the measured two output spectral SOP, we calculate Müller Matrices $R(\omega)$ for all frequencies. Then PMD vector is calculated from the matrix $R_\Delta = R(\omega+\Delta\omega)R^T(\omega)$ [7]. More specifically [7]:

$$\cos\phi = (TrR_\Delta - 1)/2 \tag{3.6}$$

$$\begin{aligned} r_1 \sin\phi &= (R_{\Delta 23} - R_{\Delta 32})/2 \\ r_2 \sin\phi &= (R_{\Delta 31} - R_{\Delta 13})/2 \\ r_3 \sin\phi &= (R_{\Delta 12} - R_{\Delta 21})/2 \end{aligned} \tag{3.7}$$

Where TrR_Δ and $R_{\Delta ij}$ are the trace and elements of the matrix R_Δ respectively. DGD is given by [7]:

$$\Delta\tau = \phi/\Delta\omega \tag{3.8}$$

and PSP is (r_1, r_2, r_3). We also found that if we release the limit that the input SOP must be two linear SOP include 0 degree and another arbitrary one except 90 degree, and just launch two arbitrary different SOPs instead as long as they are not orthogonal, we get a pseudo Müller matrix $R'(\omega)$ using the exactly same calculation. However, $R'(\omega+\Delta\omega)R'^T(\omega)$ still gives the right PMD vector. And this make MMM even more convenient in PMD measurement. In the data processing, $\Delta\omega$ need to satisfy $\Delta\tau\Delta\omega < \pi$ [7] to prevent higher order PMD effects. The noise effect can be reduced in two ways [7]: (1) choose large angle (90 degrees on the Poincarè sphere is the best) between two input SOPs on Poincarè sphere. (2) make $\Delta\tau\Delta\omega$ large, for example $\sim \pi/2$.

3.2 PMD Measurement Results

3.2.1 1-section PMF

The polarization mode dispersion (PMD) measurement results of a 1-section polarization maintaining fiber (PMF) are shown in figure 3.4. We measured a short piece (12.08 meters) of PMF with 16.7 ps estimated differential group delay (DGD) and a long one (66.23 meters) with 91.6 ps DGD. For the short piece the measured mean DGD is 1.7% different than the expected value, and the standard deviation (STD) is 1.7% of measured mean DGD. The PSPs converge to one point with the mean deviation of

2.1° on Poincarè sphere. For the long piece, the measurement result is also accurate, as shown in figure 3.4(c) and (d). The mean DGD is only 0.3% different from the expected value and the STD is only 1.6% of measured mean DGD. The PSPs are close to a single point with standard deviation of only 1.2°. All these measurements show that for the 1-section PMF, our measurements are accurate for both small PMD and large PMD (~90 ps).

3.2.2 2-section PMF

Measurement results of 2-section emulators are shown in figure 3.5. We splice up two different 2-section PMFs (8.96 m+11.04 m, and 45.23 m+21.00 m). In both cases, the angle between fast axes is 40 degree. Here the DGDs are expected to be 21.3 ps and 73.4 ps respectively. For the shorter fiber sample, the mean experimental DGD is only 1.0% different from the expected value, and the STD of the DGD measurement is only 2.7% of measured mean DGD. Moreover the PSP trajectory makes ~2.5 revolutions around a circle as expected (the number of revolutions can be calculated by $\Delta\omega\Delta nL_2/(2\pi c)$), and the radius is within 0.4% of the value predicted by equation 3.4 on the basis of the known splice angle and the relative DGDs of the two fibers. For the long fiber sample, the DGD has only 1.3% difference from the expected value, and the STD is only 3.2% of measured mean DGD. The trajectory makes ~5 traces around a circle, and the radius is within 3.6% of the expected value.

3.2.3 3-section PMF

Measurement results for 3-section emulators are shown in figure 3.6. We spliced together two different 3-section PMFs (4.57 m +11.91 m+ 4.95 m, and 45.23 m+ 20.95 m+12.03 m). For each 3-section PMF, the fast axis offset angles at two junctions are both 40 degree. For concatenations of three sections of PMF, the frequency-dependent DGD is predicted to be periodic. Though the shape of periodic curve is determined using knowledge of the fiber lengths and splice angles, the start point of the curve (the 'phase') is unknown. We tune the start point of the predicted curve to fit the measurement result for comparison. For both the shorter and longer fiber sample, the measured DGD shows good agreement with the predicted curve. The mean difference between measured and predicted DGD spectra is 0.4 ps (1.8% of 22 ps estimated mean DGD) for the shorter emulator and 3.0 ps (3.8% of 77 ps estimated mean DGD) for the long one.

For the VIPA setup, measurement errors arise from two additional factors. First since the focused spots at the camera are non-Gaussian in shape, and because spectra map nonlinearly onto the camera sensing array (these effects are inherent to VIPA operation), 60% to 80% of the power of any single frequency falls on its corresponding camera pixel; the remaining power falls on adjacent pixels as crosstalk. Second inaccuracy in the calibration of the frequency mapping onto the camera pixels can also affect experimental results. Nevertheless, our results show that excellent measurement accuracy is maintained in this high-resolution VIPA-based setup.

3.3 Conclusions

In summary, we have successfully applied our fast wavelength-parallel spectral polarimetry technology for broadband PMD measurement using Müller matrix method (MMM) algorithms. We have particularly focused on evaluating the accuracy of our PMD vector measurement results. Our findings indicate that the spectral polarimetry data are of sufficient quality to permit accurate extraction of the PMD spectrum. The spectral polarimetry approach allows fast (potentially on a few milliseconds scale) and efficient measurement of frequency-dependent PMD vectors.

An important point is that the spectral polarimetry approach can be scaled for different optical bandwidths and spectral resolutions via choice of the spectral disperser. By using a VIPA spectral disperser, a higher resolution (~3 GHz/pixel) is obtained over a 200 GHz band. This has potential to be used for PMD sensing in optical fiber communication systems at 40 Gbit/s and beyond, as the work in chapter 4. In the future, by using a two dimensional VIPA-grating spectral disperser [35], fast PMD measurement of over 1000 frequency samples spanning essentially the full C band should be possible.

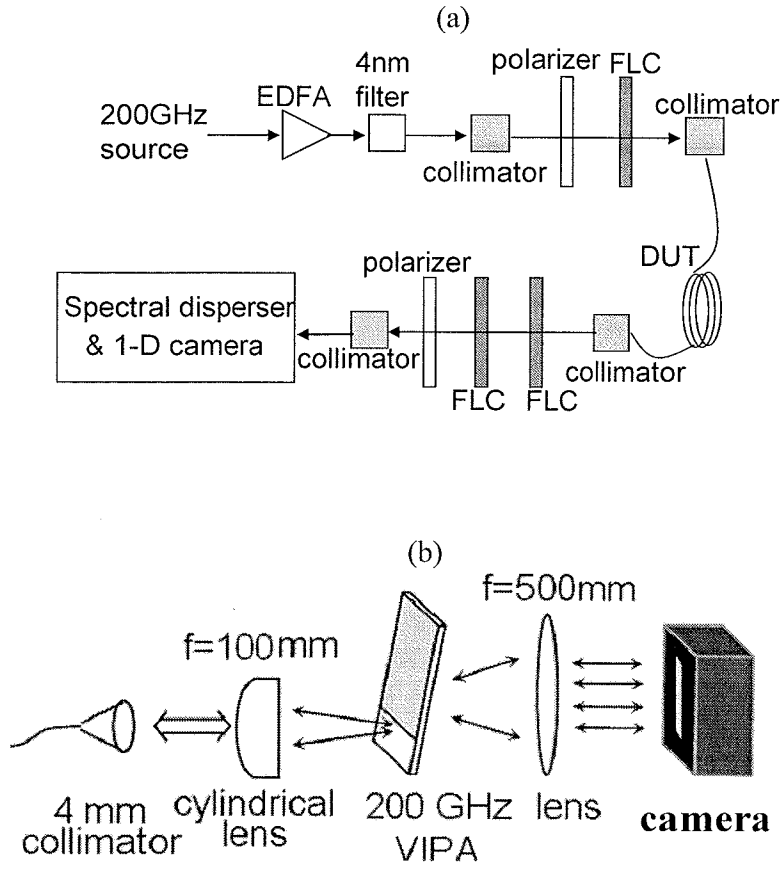

Fig. 3.1 High spectral resolution measurement setup: (a) full setup; (b) VIPA (virtually imaged phased array) spectral disperser.

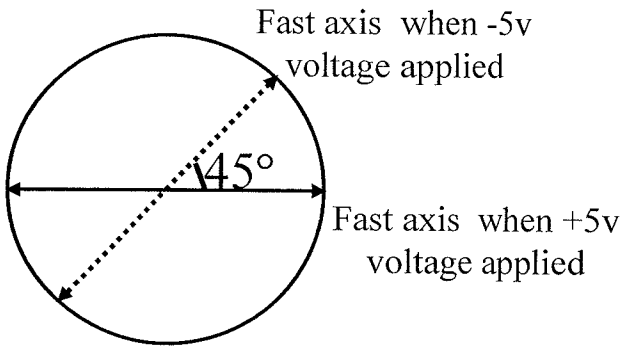

Figure 3.2 Ferroelectric liquid crystal (FLC) cell

Table 3.1
Truth table for SOP component selector

First λ /4 FLC fast axis	Second λ /4 FLC fast axis	Polarizer	SOP component selected
90 ° (-5v)	0 ° (+5v)	0°	0°
135 ° (+5v)	135 ° (- 5v)		90°
90 ° (- 5v)	135 ° (- 5v)		45°
135 ° (+5v)	0 ° (+ 5v)		RHC

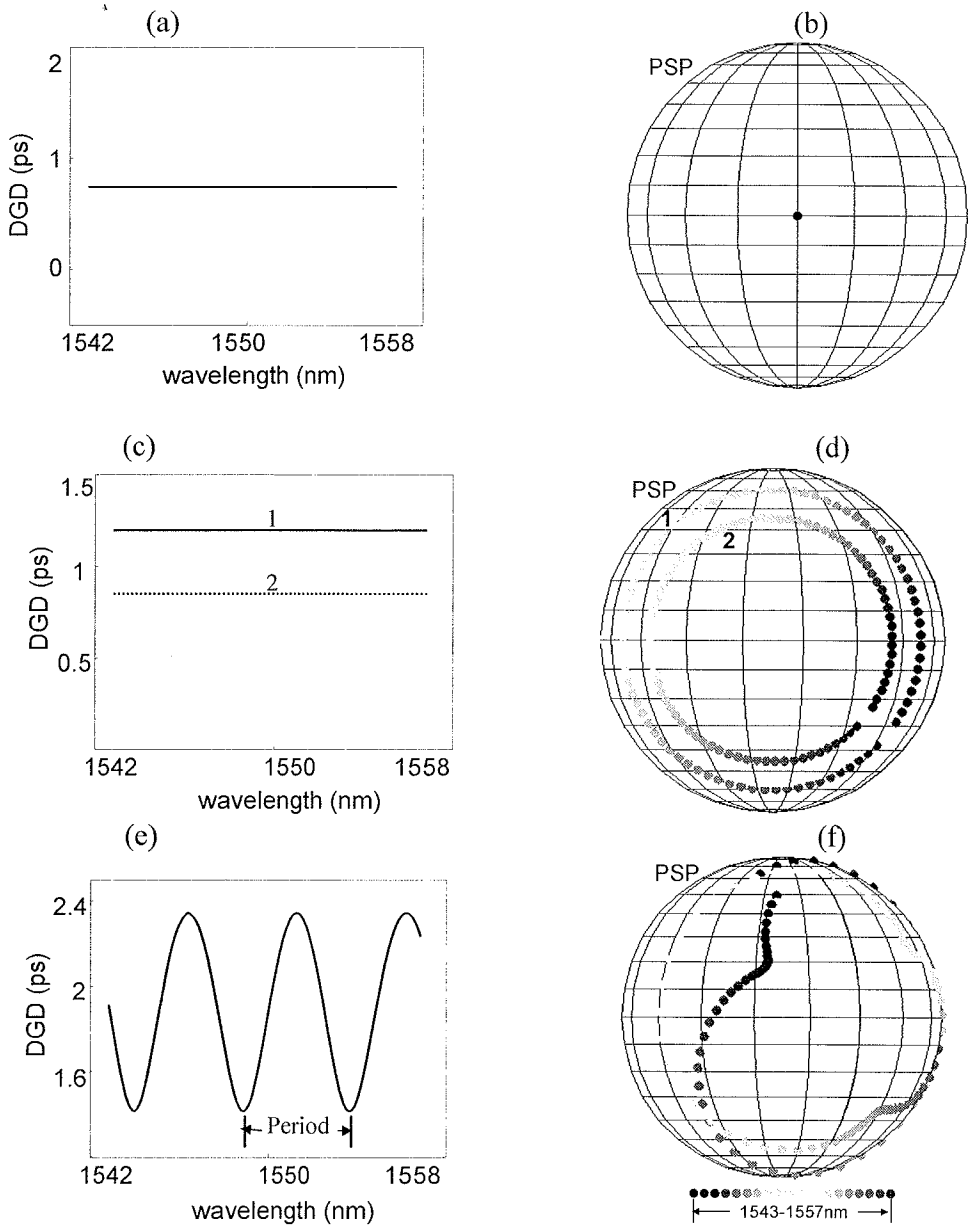

Fig. 3.3 DGD (differential group delay) and PSP (principal state of polarization) by simulation: (a)-(b) illustrate a 1-section emulator; (c)-(d) 2-section emulator, where we put two cases together. Case 1 stands for the 70 cm + 40 cm PMF (polarization maintaining fiber) concatenation with 45 degree fast axes offset. In case 2, the first PMF section is shortened from 70 cm to 40 cm to get 40cm+40cm concatenation and the fast axis offset is left unchanged. (e)-(f) 3-section emulator (59.2 cm+118.5 cm+83 cm, two fast axes offsets are both 45 degree.)

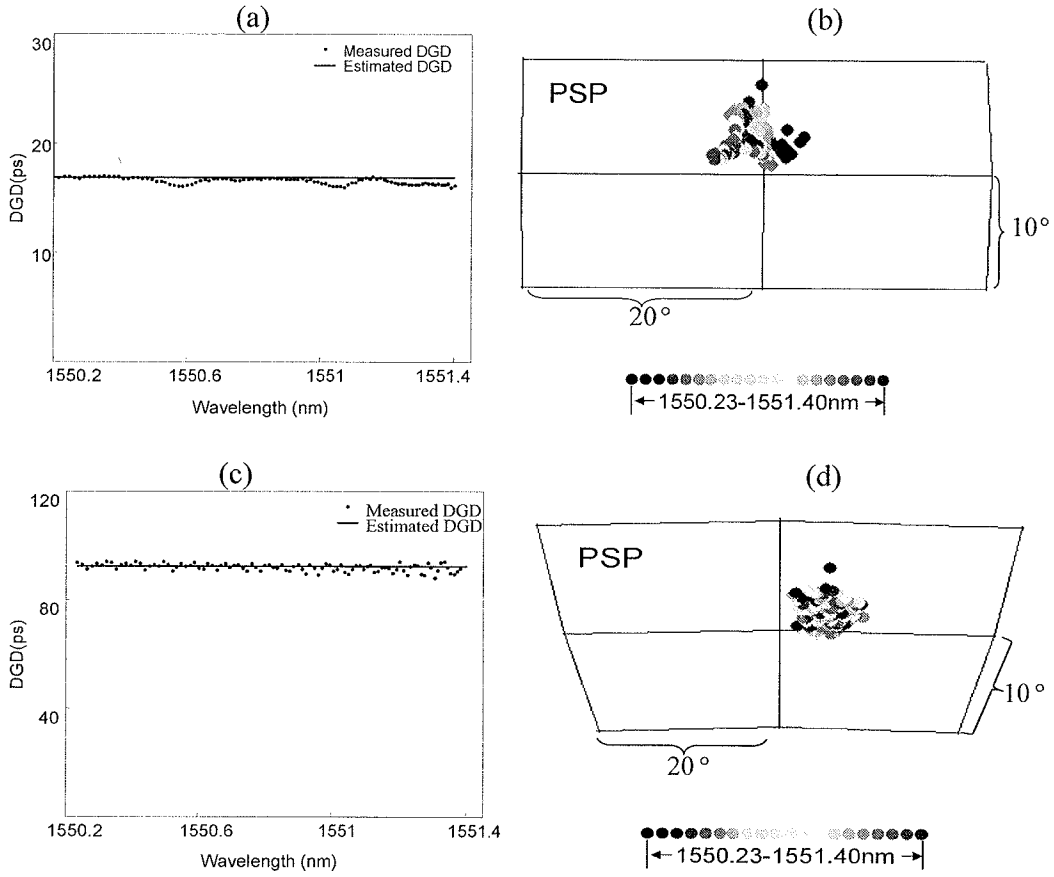

Figure 3.4 PMD vector measurement results for 1-section emulator: (a) DGD (differential group delay) and (b) PSP vector plotted on the Poincarè sphere for a short PMF (polarization maintaining fiber) with estimated 16.7 ps DGD; (c) and (d) are DGD and PSP respectively for a long PMF with estimated 91.6 ps DGD

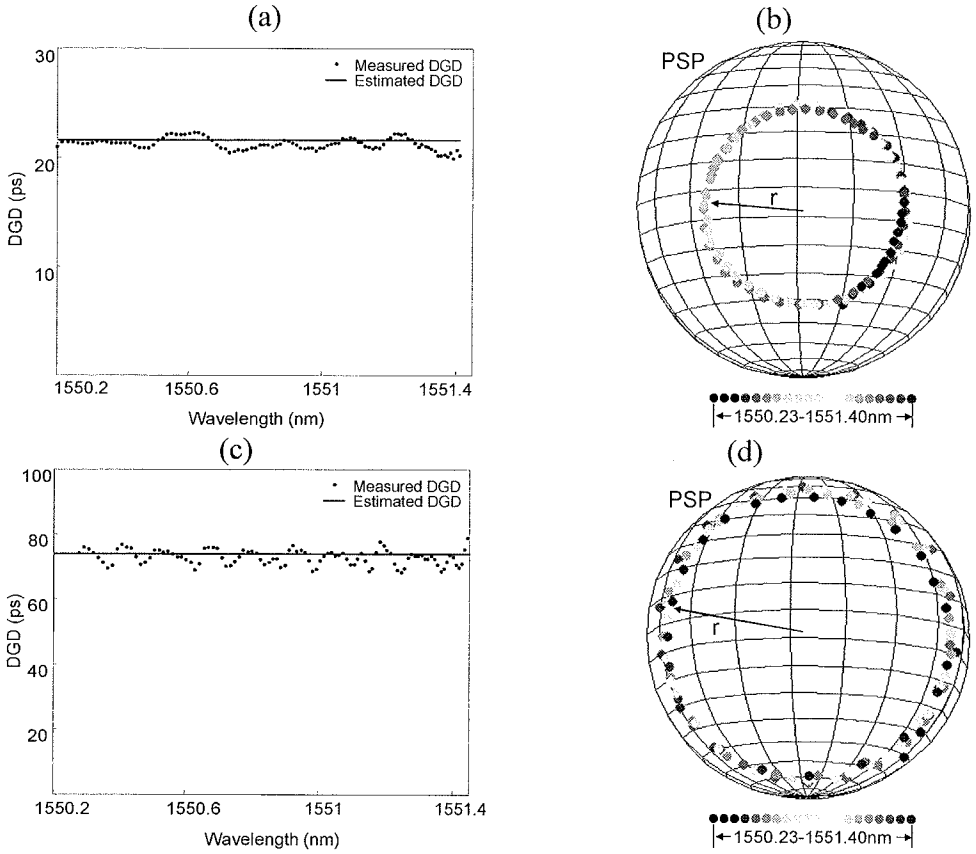

Figure 3.5 PMD vector measurement results for 2-section emulators: (a) and (b) are DGD (differential group delay) and PSP (principal state of polarization) respectively for the emulator with estimated 21.3 ps DGD. (c) and (d) are DGD and PSP respectively for the emulator with estimated 73.4 ps DGD.

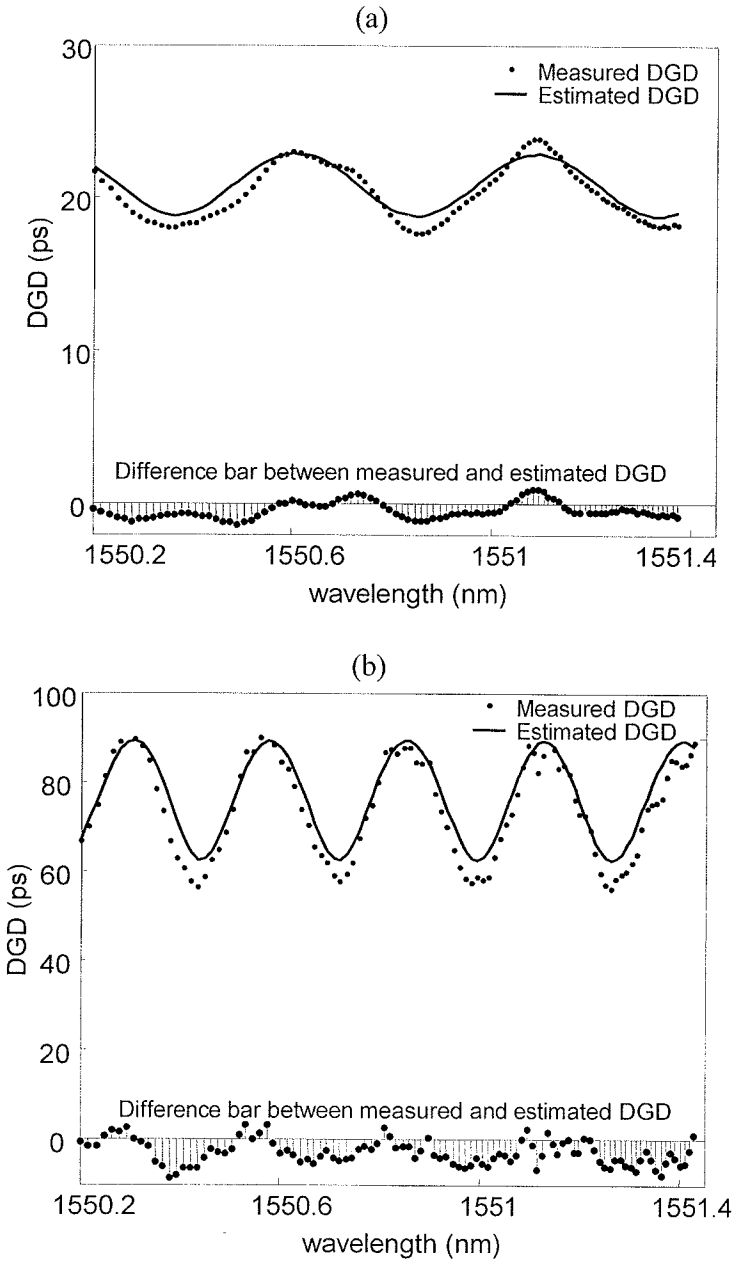

Fig. 3.6 PMD vector measurement results for 3-section emulators: DGD (differential group delay) for (a) short and (b) long emulator.

4. PMD COMPENSATION IN 10 Gbit/s×4 OPTICAL TIME DIVISON MULTIPLEXING OPTICAL FIBER COMMUNICATION SYSTEMS

Polarization mode dispersion (PMD) is considered a major obstacle for ultrahigh-capacity fiber communication systems at 40 Gbaud/s and above. Although some electrical PMD compensation (PMDC) is possible, it is complex and expensive for high symbol rates, and to date experiments reaching to 40 Gbaud/s are limited. Furthermore, most research on PMDC, either electrical or optical, has been limited to the first- or second-order PMD regime, valid only for distortions small compared to the bit period or pulse width. Here for the first time we demonstrate all-order optical PMDC in a lightwave system experiment at 40 Gbaud/s (realized via 10 Gbit/s ×4 optical time division multiplexing (OTDM) for compatibility with the speed of our bit error rate tester). In this chapter we give the experimental details. In section 4.1 we discuss the experimental setup including the whole picture and the details of each module. In Section 4.2 we shows the PMD compensation scheme. Experimental results are in Section 4.3. Finally, we conclude in section 4.4.

4.1 The Experimental Setup

4.1.1 The structure of the full system setup

As shown in figure 4.1, our experimental setup includes a transmitter, a PMD emulator, and a receiver. The transmitter comprises a 10GHz short pulse source, a modulator, and an optical 10G-to-40G OTDM multiplexer. The receiver includes PMD sensing optics and the PMD compensator, a 40G-to-10G OTDM demultiplexer, a 10 GHz photodiode, and a bit error rate (BER) test set..

The clock of the 10 G pulse source, modulator, DEMUX and BER testing are the same. The 10 G pulse source from another room is introduced to the setup by a 50-meter single mode fiber, which is attached on the ceiling tightly to make polarization stable. A small power portion of this source is received by a 20 GHz photodiode to

generate clock signal. This clock is used as external clock for the BER test instrument, which provides all the other clocks needed in the setup.

4.1.2 10 GHz source

For 10Gbit/s $\times 4$ optical time division multiplexing (OTDM), we need to multiplex four 10Gbit/s channels in time domain. The interference between channels is a concern, which places requirements on the 10 Ghz source.

To be simple, we illustrate the interference using two neighbor channels here. We assume that two channels have the same peak I_p and tail I_t, as seen in fig. 4.2. For channel #1, the superposition of its peak (with phase φ_p) and channel #2's tail (with phase φ_t) gives new peak I_p' of Channel #1:

$$\begin{aligned} I_p' &= \left|\sqrt{I_p} + \sqrt{I_t} e^{j(\varphi_p - \varphi_t)}\right|^2 \\ &= I_p + 2\sqrt{I_p}\sqrt{I_t}\cos(\varphi_p - \varphi_t) + I_t \end{aligned} \tag{4.1}$$

It contains three parts. The second part $2\sqrt{I_p}\sqrt{I_t}\cos(\varphi_p - \varphi_t)$ is called interferometric crosstalk. The third part I_t is called inter-symbol crosstalk, which is much smaller compared with the second part and thus ignored. The interferometric crosstalk changes due to the random variance of the phase difference $\varphi_p - \varphi_t$. If the peak to tail extinction ratio I_p / I_t is 20 dB, then I_p' variation is between -19% and 21%, which is not minor. If the ratio is 30 dB, then I_p' variation is between -6.2% and 6.4%, which may be bearable. This shows that high peak to tail extinction ratio is required to reduce interfermoetric crosstalk.

Considering interferometric crosstalk, the most relaxed requirement (1dB BER power penalty) for pulse source for 4 x 10Gbit/s OTDM is [39]: (1) Pulse tail extinction ratio 27 db; (2) pulse FWHM=0.4 x timeslot (that is 10ps). Another requirement is the 200 GHz bandwidth of virtually imaged phased array (VIPA) in the PMD sensing and compensation module.

We try to find the appropriate source. First, we tried to use pulse-carving technique on CW laser by using intensity modulators. Mach-Zehnder intensity modulators are in abundance in our lab, so they are considered. However, we found that even concatenation of two modulators could not give narrow enough pulse and high enough peak to tail extinction ratio. Instead, we use this to build DEMUX later. Electrical absorption modulator (EA) for pulse carving is another choice. However, it is too expensive, and cannot guarantee the requirements.

Then we take advantage of the broadband comb source in our lab [40]. It starts with a CW laser, which is strongly modulated at 10 GHz to form a comb, then phase compensated via a pulse shaper to generate ~3 ps FWHM pulses . We slice the 160GHz band (shown in figure 4.3) from that by a pulse shaper and hope that the pulse can work. Unfortunately, the peak to tail extinction ratio is not large enough (shown in figure 4.4) because the profile of the combs is not smooth. To solve this problem and generate smooth spectrum profile, we amplified the ~3 ps FWHM pulses and perform adiabatic soliton compression in a dispersion decreasing fiber. As a result generates a broad flat spectrum, from which we slice a smooth spectrum of ~120 GHz bandwidth FWHM, as shown in figure 4.5. By autocorrelation measurement results in figure 4.6, this pulse has high peak to tail extinction ratio and narrow width (~5.9 ps FWHM), which is good enough for our 10 Gbit/s ×4 OTDM.

4.1.3 Data modulation

We use bit error rate (BER) test instrument to generate a PRBS data as 10 GHz RF signal. Later the data received will be sent back to BER test instrument so that it can compare with the transmitted data for BER test. The transmitted 10 GHz RF signal is amplified by a RF amplifier and then applied to an optical intensity modulator to add OOK (on and off keying) code to the 10 GHz optical pulse source. This modulation is polarization sensitive. So a polarization controller is used before the modulator input port, to ensure minimum transmission loss (~8 dB). The best way to treat the polarization is to splice polarization maintaining fiber (PMF) pigtail to the input port of the modulator, and use a polarization controller an a inline polarizer before the input PMF pigtail.

4.1.4 Carrier suppression

As for OOK code modulated on 10 Gbit×4 OTDM signal, the spectrum has carrier peaks with 10GHz apart between peaks. The low intensity portion between peaks contains the information the signal carries. These carrier peaks are undesirable to our frequency-parallel PMD sensing for three reasons:

(1) We use sensing array with 128 pixels to sense the 200 GHz frequency band dispersed to free space, and the size of light beam covers 2 pixels. Due to this, the carrier peaks affect the intensity on its neighbor pixels significantly, which are supposed

to sense the low intensity parts of the spectrum. As a result, only the peaks can be possibly measured accurately.

(2) Because four channels have random phase, the energy distribution between peaks changes randomly and faster than SOP measurement speed. Moreover, occasionally one carrier peak can become very high and possibly damage sensing camera.

(3) Even if the carrier peaks are stable, they cannot be measured correctly because of virtually imaged phased array (VIPA) as spectral disperser before sensing array. With VIPA, the intensity of the peaks varies up to 18%. We test other kinds of light source. For single wavelength (tens of MHz linewidth) from CW laser, the variation is also up to 18%. If we send the CW laser beam directly to sensor, without VIPA, it shows less than 0.35% variation. Because CW laser itself is stable with its frequency and intensity, we confirm that that VIPA introduces variation. We also confirm that ASE source can work with VIPA setup, with only 1% intensity variation. Its spectrum is continuous and much smoother than the OTDM signal with carrier peaks. So the possible reason is the interference caused by two faces of VIPA, which affect CW laser (with narrow linewidth and long coherent length) and 10 Gbit×4 OTDM signal (with narrow linewidth for the carriers and long coherent length), but does not affect ASE source (with continuous spectrum and short coherent length). This also gives us the idea of suppressing the carriers in OTDM signal to get continuous spectrum like ASE source.

We intend to choose an appropriate modulation format to realize carrier suppression. Figure 4.7 shows the spectrum of three different modulation format [41]: RZ-OOK (return-to-zero on/off keying), CSRZ-OOK (carrier-suppressed return-to-zero on/off keying), RZ-DPSK(return-to-zero differential phase shift keying). We also show the details of the intensity and phase modulation on all these three formats, as in table 4.1. RZ-OOK, is what we used to add code the 10 G pulses, but as shown in figure 4.7 (a), it has carriers. CSRZ-OOK is so called carrier suppressed, but it only means suppressing the carrier at the center by moving all the carriers for 5 GHz (as for 10 G source). All the carries still exist, as shown in fig 4.7 (b). RZ-DPSK performs coding by phase modulation (differential phase shift keying), and its carriers all disappear as in figure 4.7 (c). Comparing the modulation details of these three modulation in table 4.1, we conclude that random 0, π phase between bits are the key to suppress all carriers. It is also confirmed by simulation on computers.

Based on RZ-OOK modulation we already adopt, we use another phase modulator to add pseudorandom 0, π phase to each bit. The carriers are successfully

suppressed, as shown in figure 4.8. It is worth mentioning that pseudorandom 0, π phase is critical here, and thus should be finely tuned. From simulation on computers, even pseudorandom 0, 0.95π phase leaves a large portion of each carrier unsuppressed.

We do not choose RZ-DPSK modulation, though this format itself is totally carrier suppressed and thus needs only one modulator. It is because we use adiabatic soliton compression in a dispersion decreasing fiber to help generate the source, and this degrades high signal to noise ratio especially for DPSK modulation format [42], but not for OOK format.

4.1.5 10Gbit/s to 4x10Gbit/s OTDM multiplexer

To realize 10G-to-40G multiplexing in time domain means that four channels are coupled together and channel 2, 3, 4 have random number of bits plus 25 ps, 50 ps, 75 ps delay to channel 1 respectively.

We build an optical setup for 10 G to 40 G MUX. As shown in figure 4.5, the input 10 G pulse goes to the circulator port 1, and then goes out of the circulator port 2 to a 1:4 coupler. Thus, we produce four channels. For each channel, the light goes to free space by a collimator, and then it is reflected back by a mirror. Each mirror is on a translation stage so that we can finely tune the mirror back and forth to realize delay tuning. All four channels then come back, couple together and go out of the circulator port 3. We then put a polarizer together with polarization controller in each channel to keep each channel the same state of polarization and power. Since the interference between channels is largest if they have the same polarization, it make the test on our system more strict.

The whole MUX setup has ~18 dB loss: the 1:4 coupler has ~12 dB loss for round way pass; the collimator-mirror pair has ~4 dB loss; and the circulator and other components have ~2 dB loss in total.

4.1.6 4x10 Gbit/s OTDM to 10 Gbit/s demultiplexer

To test the signal quality of each channel, we need a demultiplexer (DEMUX) module to extract them separately. In other words, we need a time 'gate' to allow the wanted channel go through, as shown in figure 4.10. In general, people let the signal containing 4 OTDM channels go to a 1:4 coupler followed by 4 gates to DEMUX each channel independently. In our experiment, in order to save lab resources, we use only one gate, and demultiplex different channels by tuning the relative position of the time gate.

Two concatenated Mach-Zehnder intensity modulators are adopted to realize this gate. In a Mach-Zehnder modulator (MZM), the input light is divided into two branches with equal intensity, as shown in figure 4.11 (a). The two branches have different phase delay. When they combine at the output, the light intensity is a function of the phase delay difference ϕ:

$$I_{out} = I_0 \cdot (\cos(\phi/2))^2 \tag{4.2}$$

The transmission curve is shown in figure 4.11 (b). If the phase delay difference ϕ is proportional to the electrical voltage applied to the branch material ($LiNO_3$, for example), then we can use electrical signal to realize intensity modulation. For example, if we use RF signal:

$$\phi(t) = \frac{V}{V_\pi}\pi\cos(2\pi ft + \delta) + \varphi \tag{4.3}$$

then different V, f, δ and φ values can be chosen to do a variety of modulation.

To make a 40G to 10G DEMUX module, we concatenate two MZMs. The idea is to choose different parameters for them to realize a narrow enough 'gate' in time domain. It means that for a CW laser input, the output is 10 GHz pulses with an appropriate width, as shown in figure 4.12 (a). The parameters we choose are:

$$MZM1:(\frac{V_1}{V_\pi}, f_1, \delta_1, \varphi_1) = (0.5, 10GHz, 0, \frac{\pi}{2}) \tag{4.4}$$

$$MZM2:(\frac{V_2}{V_\pi}, f_2, \delta_2, \varphi_2) = (1, 10GHz, \frac{\pi}{2}, 0) \tag{4.5}$$

So for the first MZM alone, the modulation is 10 G pulses with 50 ps FWHM. For the second MZM alone, the intensity is 20 G pulses with 16.5ps FWHM. When we concatenate these two together, we get 10 G pulses with 16.5ps FWHM. This can compare with the commercial product from CIP LTD, which is electrical absorption modulator producing 15ps FWHM window. Figure 4.12 (b)-(d) show the simulation results.

We successfully realize this idea in experiment. Figure 4.13 shows the details of this DEMUX module. One 10 GHz RF signal is divided into two and given to two MZMs. Each MZM need a modulator driver to amplify the input RF signal to desired amplitude V. DC bias gives φ. We input CW laser to the setup, and use a RF fast sampling scope with a 50GHz photodiode at the output to observe the results. We tune two MZMs one by one to get the right modulation for each. Then we operate both of them, and use RF phase shifter #2 to make $\pi/2$ difference between two RF signal phase δ, or in other words, to tune relative position of the peaks of two modulation. After all

these, we can the time gate needed for DEMUX. Moreover, RF phase shifter #1 in figure 4.13 is used to tune the location of the DEMUX gate, thus we can extract different channels. Because these modulators are polarization sensitive, polarization controller and in-line polarizer are used for each.

Problem occurs later when the second modulator MZM2 has so high V_π that we do not have high enough V to satisfy $V=V_\pi$. This makes the valley of its modulation curve a distance from zero. In this situation, by modulate both MZM1 and MZM2 as seen in figure 4.14 (a), the time gate falls to zero slowly, and may allow a part of unwanted neighbor channels to go through. To solve this problem, we change the modulation parameters V and δ ($V = 0.25V_\pi, \delta = 0.75\pi$, for example) of MZM1, and make its duty ratio smaller. As shown in figure 4.14 (b), though more loss is introduced, the time gate falls to zero more quickly and thus works well as a DEMUX. As a result we get he time gate desired, as shown in figure 4.15. The optical power loss of this whole DEMUX module is ~20 dB.

4.1.7 Bit error rate (BER) test

The BER test structure at receiver module is shown in figure. 4.16. The channel under test goes to an in-line optical attenuator followed by a 1:2 coupler. One branch is detected by a 10 GHz photodiode. We amplify the electrical signal from the photodiode and send it to BER test instrument. The other branch is used to monitor the optical power. We tune the attenuator for several times, measure two branches simultaneously to get a BER vs. optical power curve.

We perform back-to-back BER test to evaluate the quality of our 10 Gbit/s×4 OTDM system test-bed built so far. We transmit light through all the modules except PMD emulator and PMD compensation. One channel is demuxed from 10 Gbit/s×1 OTDM, 10 Gbit/s×2 OTDM, 10 Gbit/s×4 OTDM (we generrate different numbers of OTDM channels at MUX) and tested respectively. The BER results is shown in figure 4.17. The BER of one channel demuxed from 10 Gbit/s×4 OTDM goes down to 10^{-10}. This shows good quality of the optical signal and its transmission in the system modules. The power penalty between one channel demuxed from 10 Gbit/s×4 OTDM and one channel demuxed from 10 Gbit/s×1 OTDM is 1.7 dB. This shows the good quality of 10G-to-40G OTDM MUX and 40G-to-10G OTDM DEMUX, as well as the compatibility of our light source with them.

4.2 PMD Sensing and Compensation Scheme

With the system test-bed built, we are ready to apply our all-order PMD compensation technique [16] in 10 Gbit/s×4 OTDM systems. In this section we give details on PMD sensing and compensation setup, and the algorithm for compensation.

4.2.1 PMD sensing and compensation setup

As in chapter 3, here we also use homemade PMD emulators. They are the concatenation of over 10 polarization maintaining fiber sections with randomly set fast axes and different lengths. So they have large all-order PMD. All channels have the same state of polarization (SOP) before going to the PMD emulator. As shown in 4.18 (a), two ferroelectric liquid crystal (FLC) cells are used to impose a sequence of four different polarization transformations onto the signal prior to the emulator, which is used to sense the frequency-dependent Jones matrix of the PMD [16, 18].

The PMD sensing and compensation module (with 19 dB loss) is shown in fig. 4.18(b). The spectrum of the input signal is dispersed in free space by a virtually imaged phase array (VIPA) [17] with 200 GHz free spectral range. A polarization insensitive beam splitter directs a portion of the signal to our fast wavelength-parallel polarimeter [37], with the remaining signal going to a 128-pixel × four-layer liquid crystal modular (LCM) array for PMD compensation [16,18]. The spectral dispersion across the pixels of the LCM array and of the 1-dimensional camera (used in PMD sensing) are carefully matched, with a value of 1.6 GHz/pixel. By sequentially transforming the launch polarization into the PMD emulator and measuring the frequency-dependent polarization of the output light for each launch, we are able to calculate the frequency-dependent Jones matrix of the emulator at each frequency sample. In the compensation process the first 3 layers of the LCM array are programmed to generate the inverse frequency-dependent Jones matrix. The 3^{rd} and 4^{th} layers also compensate isotropic spectral phase (generalized chromatic dispersion) introduced by the PMD compensation step. This combination realizes complete all-order PMDC. The details of PMD compensation algorithm will be shown later.

When we perform back-to-back system BER test, first we let the signal pass the whole system except PMD emulator and PMDC module. In BER test result, there is 1.7 dB power penalty for 1 channel demuxed from 10 Gbit/s ×4 OTDM signal compared with BER of the original 10 Gbit/s signal. Then we let the signal go through the whole system without PMD emulator but with PMDC module (set for a quiescent state). The

BER result shows 1 dB more power penalty as seen in figure 4.19. This is caused by 10% spectrum narrowing introduced by VIPA passband, as shown in figure 4.20. We use the latter back-to-back BER result as our baseline to estimate the quality of PMDC after a PMD emulator is inserted.

4.2.2 PMD compensation algorithm

The idea of the PMD compensation method is to measure the frequency dependent Jones matrix of the fiber link, and then use 4 layer liquid crystal modulators (LCM) to generate the inverse of this Jones matrix, and thus realize all-order PMD compensation. The fast axes of these four LCM layers are 0°-45°-0°-90°.

Without polarization dependant loss, the Jones matrix a fiber link can be written as [28]:

$$U_f = \begin{bmatrix} \cos\theta e^{j\phi} & \sin\theta e^{j\psi} \\ -\sin\theta e^{-j\psi} & \cos\theta e^{-j\phi} \end{bmatrix} \tag{4.6}$$

Where θ, ϕ and ψ are frequency dependant parameters.

We give two known input SOP (for example, 0^o and RHC), and measure the two output SOPs for each wavelength using wavelength parallel parameter. θ, ϕ and ψ can be calculated analytically from the output SOPs [43].

Now we use first three layer LCMs to generate the inverse Jones matrix, which is in the form of the product of three elementary rotation matrix realized by these three LCM layers respectively:

$$U_f^{-1} = \begin{bmatrix} \exp(-j\theta_3) & 0 \\ 0 & \exp(j\theta_3) \end{bmatrix} \begin{bmatrix} \cos\theta_2 & -j\sin\theta_2 \\ -j\sin\theta_2 & \cos\theta_2 \end{bmatrix} \begin{bmatrix} \exp(-j\theta_1) & 0 \\ 0 & \exp(j\theta_1) \end{bmatrix} \tag{4.7}$$

where $\theta_1 = (\phi+\psi)/2 + \pi/4$, $\theta_2 = -\theta$, $\theta_3 = (\phi-\psi)/2 - \pi/4$ by calculation. After generating the inverse Jones matrix, these 3 layers introduce spectral phase $-(\theta_1+\theta_2+\theta_3)$. Then the four layer and the third layer are used to compensate this extra phase, and this phase compensation is polarization insensitive. It is worth noting that the phase of the third layer is the superposition of two part: one is for the inverse Jones matrix, and the other is to compensate the introduced extra spectral phase. After the operation of all four layer LCM, Jones matrix of the fiber link is corrected, and thus all-order PMD compensation is realized.

4.3 PMD Compensation Results

We performed PMD compensation (PMDC) in four cases with different PMD emulator. The mean differential group delay (DGD) of them are: (1) 29.1 ps; (2) 45.3 ps; (3) 57.5 ps: (4) 58.8 ps. In PMD measurement [18], the output SOP vs. frequency for these four emulators (one launch SOP) is shown in figure 4.21, and the PMD results are shown in figure 4.22 (a)-(d) as DGD vs. wavelength. In all these cases, DGD has large mean value and varies in large range compared with 5.9 ps width of the signal pulse and the symbol period 25 ps. This puts us well into the regime where Taylor series approximations to the PMD break down and all-order PMD must be considered.

In both cases a 50GHz photodiode is used before the 40G-to-10G demultiplexer to measure eye diagrams, both with and without PMDC. Results are shown both for a single 10Gbit/s input channel and for the 10 Gbit/s ×4 OTDM signal. A 10 G photodiode is used to measure bit error rates after a single 10G channel is demuxed from the 10Gbit/s ×4 OTDM signal.

The PMDC result of case 1 is shown in figure. 4.23. With 29.1 ps mean DGD, 10 Gbit/s signal is broadened and distorted, as shown in figure 4.23 (a). For 10 Gbit/s×4 OTDM in figure 4.23 (c), intersymbol interference (ISI) make the eye become thick. And BER for one channel measured with figure 4.23 (e) is only 10^{-3}. After PMDC, the 10G pulse is compensated to its original shape (as shown in figure 4.23 (b)), and clean eyes are recovered (as shown if figure 4.23 (d) and (f)). From figure 4.24, the BER is improved significantly after PMDC. It has 2-2.5 dB power penalty compared back-to-back case down to a BER floor of ~10^{-9}.

The PMDC results for case 2 are shown in figure 4.25. For this emulator, DGD vs. wavelength varies over a 30-80 ps range with 45.3 ps mean value. This broadens and distorts the 10 Gbit/s signal, figure 4.25 (a). For 10 Gbit/s×4 OTDM, figure 4.25 (c), strong intersymbol interference (ISI) degrades the eye. The BER for a single channel after demux is very poor (~0.2-0.4). After PMDC, the 10 G pulse is compensated to its original shape, figure 4.25 (b), and clean eyes are recovered for 40 Gbit/s operation, figure 4.25 (d). From figure 4.26, the BER is improved significantly after PMDC. Although there is a 2.5 dB power penalty, error rates down to a few times 10^{-9} are obtained.

Results for case 3 are shown in figure 4.27. Here the DGD vs. wavelength varies between 10-100 ps, with 57.5 ps mean DGD. The original 5.9 ps pulse is broadened to approximately the 100ps range. For 10 Gbit/s×4 OTDM in figure 4.27 (c), the intersymbol interference (ISI) is so strong that the eyes completely close, and the BER is essentially 0.5. After PMDC, the 10 G pulse is compensated to its original shape, and clean eyes are recovered for the 40 G signal, figure 4.27 (b) and (d). From figure 4.28 the BER goes down to a floor of $\sim 10^{-6}$, well into the range in which FEC is possible, with ~3 dB power penalty compared to back-to-back.

Case 4 is shown in figure 4.29. DGD vs. wavelength varies in 20-130 ps range with 58.8 ps mean value. The original 5.9 ps pulse is broadened to approximately 150 ps range. The eyes completely close, and BER is essentially 0.5. After PMDC, the 10 G pulse is compensated almost to its original shape (as shown in figure 4.29 (b)). Though eyes for 10Gbit/s×4 OTDM is recovered, the BER only reach the floor of $\sim 10^{-3}$, as shown in figure 4.30.

Although substantial PMD compensation is achieved, it is also clear that some degradation remains. We attribute this to limited spectral resolution, both in sensing and compensation. Although the spectrum is dispersed to 1.6 GHz/pixel, the actual beam size for any single frequency covers two pixels, for ~3 GHz resolution. When PMD is large, SOP varies very rapidly with frequency. Recall that in the sensing we need to measure 4 output SOP vs. frequency (pixel). For each SOP we need to measure intensity of four SOP components (0^0, 45^0, 90^0, RHC) vs. frequency. In figure 4.31 we show measured intensity vs. pixel for our polarization sensor for the 0^0 linear SOP component. Finer features are observed as the mean DGD increases. For example, for figure 4.31 (d) the feature near pixel 80 is only three pixels wide. Such features approach the spectral resolution limit of our apparatus and introduce inaccuracy. The ability of the compensation module to control the frequency-dependent Jones matrix is limited by the same spectral resolution limits. Although the PMDC data for individual 10 Gbit/s channels looks ok, spectral resolution issues contribute to slight reshaping of our pulses, which as a result no longer fully conform to the strict interferometric crosstalk requirements in OTDM systems [39].

In the figures mentioned above, the eye diagrams are taken when the polarization switching used for PMD sensing is switched off. For figure 4.32 (b), we continuously switch between two polarization states at 2 kHz frequency during the PMDC operation (using the case 1 emulator). As in previous isolated pulse experiments [16], polarization switching does not significantly affect the recovered pulse compared with

figure 4.32 (a) which is without switching. This provides evidence that the in-line polarization switching we use at the input, in order to allow real-time Jones matrix sensing, is compatible with simultaneous data transmission.

4.4 Conclusions

We experimentally demonstrate feed-forward all-order optical PMD compensation in a 10 Gbit/s×4 OTDM system with very large PMD (mean DGD >50ps) using a hyperfine resolution pulse shaper provisioned with a four-layer liquid crystal modulator array and frequency-dependent Jones matrix sensing. This shows the possibility of PMDC at 40 G/s symbol rate for distortions so large their compensation is usually viewed as intractable. Furthermore, our all-optical approach can readily be extended to higher symbol rates (pulses down to the sub-ps range [18]).

In this 10 Gbit/s×4 OTDM system experiments, there are some problems that need to be paid attention to:

(1) The quality of the light source. We use a diabatic soliton compression in a dispersion decreasing fiber (DDF) generates a broad flat spectrum for slicing a nice Gaussian like spectrum. The OSNR of light needs to be large enough before it goes to DDF. Otherwise, we get very bad back-to-back BER test result even if we optimize the rest of the system.

(2) Clock synchronization. All the clocks should be exactly the same, otherwise modulation and BER test is not possible. We extract the clock from the light source (should be before DDF fiber), send it to BER test instrument (BERT), and generate all the RF signals with this clock.

(3) RF signal management. We have 4 modulators in total, and need 4 RF signal (two 3dB RF power splitter are used to make this possible). Each modulator needs several DC voltage supplies, so do the RF amplifiers. There are about 20 DC supplies, and all of them should be very clearly marked for easy access. Attention is highly needed not to damage the electric components.

(4) Loss management. There are 5 EDFAs in total in this experiment to compensate the optical power loss. They are placed in appropriate locations so that the power should not be too small before input of each EDFA. EDFA also introduce extra noise that exists outside the 200 GHz band of our signal and will overlap as other FSRs

in VIPA setup to make PMD sensing inaccurate. This should be filtered out before PMD sensing module.

(5) Calibration of 4-layer LCM. When we operate LCM by apply different voltage level to generate the phase desired, we need a precalibrated phase vs. voltage curve. This is much more difficult for 4-layer LCM than 1-layer LCM. A special strategy is designed for the calibration.

(6) Stabilization of the whole system. Because our experiments handle polarization, which is sensitive with the environment, we need to make the whole system stable. All the single mode fiber (SMF) pigtails are taped to optical table or other stable objects. All the modulators have polarization controller and polarizer before the input if possible. The PMD emulators are put in a temperature-controlled foam box to avoid temperature change and other disturbances. Even so, the experiment condition still changes. We need to check the whole setup each time before taking data.

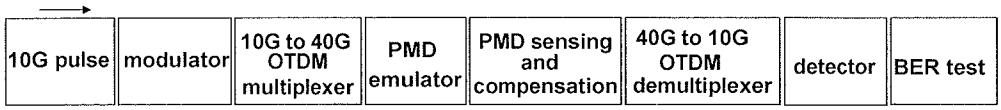

Fig. 4.1 Full setup for PMD compensation in 10 Gbit/s x 4 OTDM systems

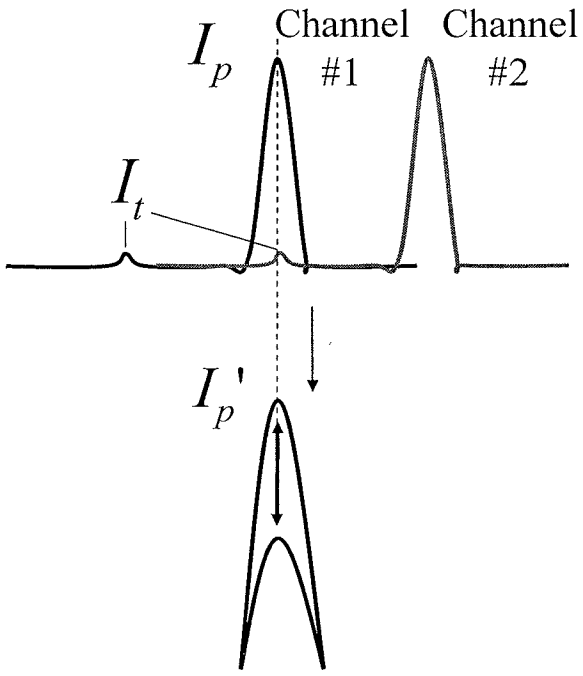

Fig. 4.2 Interference between two OTDM channels.

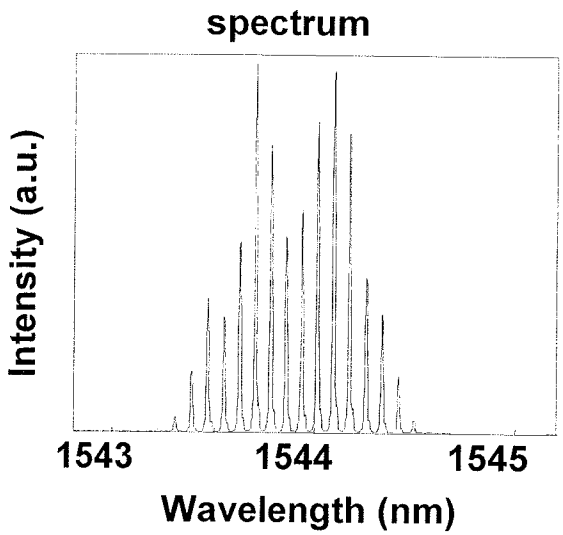

Fig. 4.3 Spectrum sliced from broadband comb source.

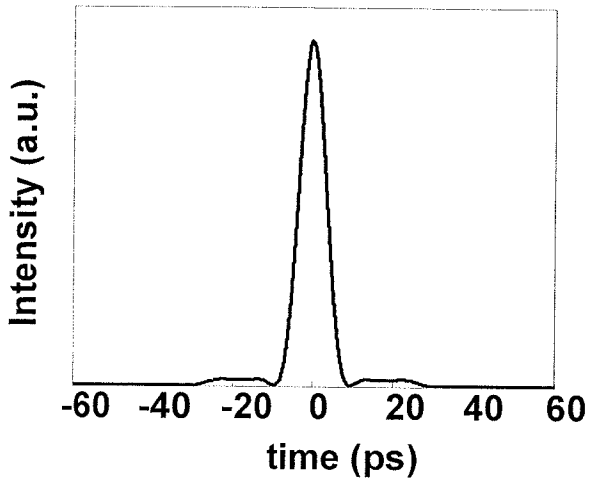

Fig. 4.4 Estimated pulse shape by Fourier transform on the spectrum of figure 4.3.

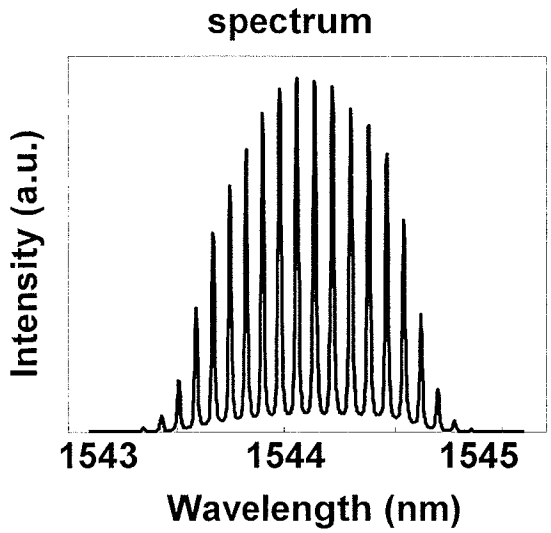

Fig. 4.5 10 GHz pulse source with smooth Gaussian like profile spectrum.

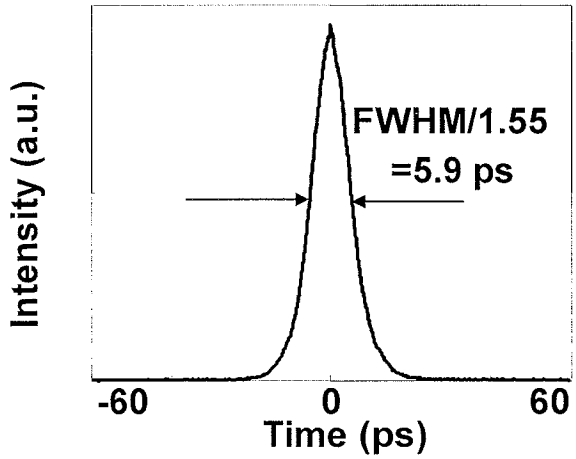

Fig. 4.6 Auto-correlation measurement of 10 GHz pulse (its spectrum is in figure 4.5) source shows 5.9 ps FWHM.

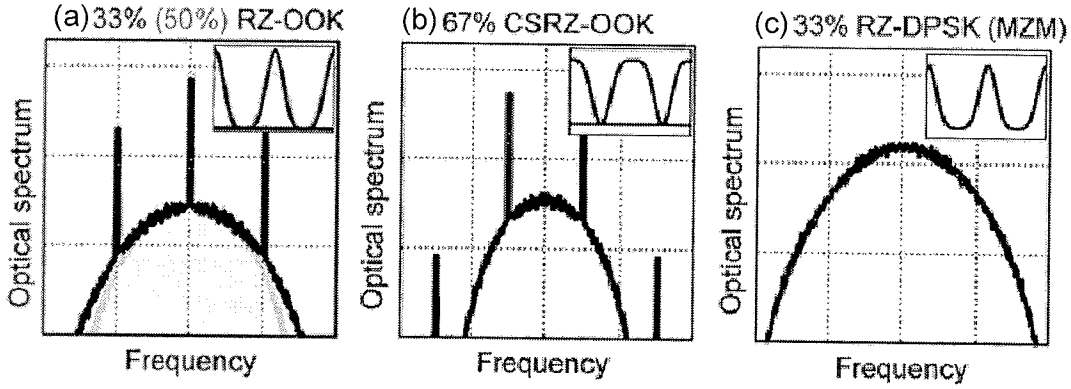

Fig. 4.7 Three different modulation formats (figures cited from [41]): (a) RZ-OOK (b)CSRZ-OOK (c) RZ-DPSK

Table 4.1
Three Modulation Formats

	RZ-OOK	CSRZ-OOK	RZ-DPSK
Intensity modulation	Random 1,0	Random 1,0	constant
Phase modulation	constant	0,π, 0,π…	Random 0,π

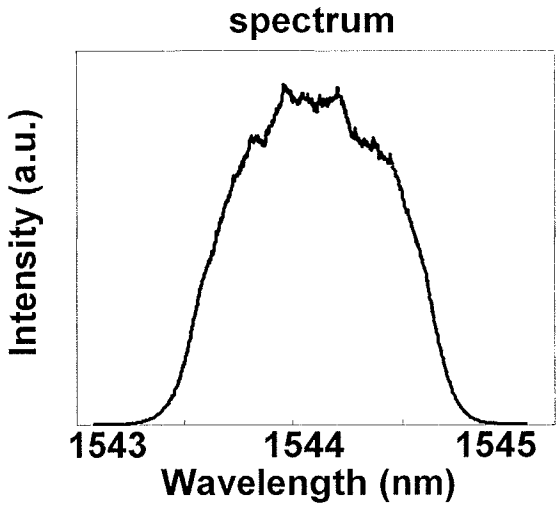

Fig. 4.8 10 Gbit/s signal spectrum after carrier suppression.

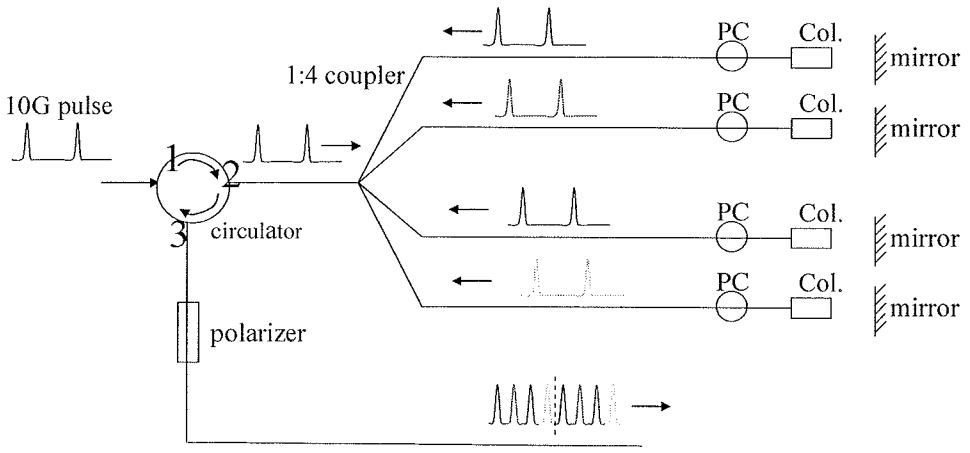

Fig. 4.9 The structure of 10G-to-40G MUX module

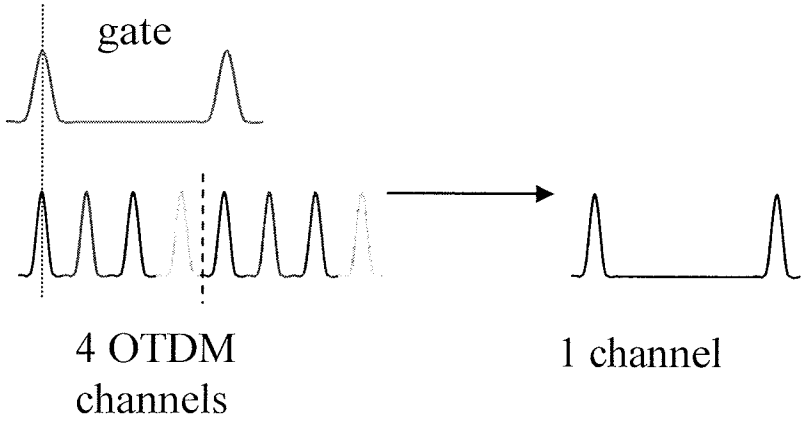

Fig. 4.10 An optical time gate to DEMUX one channel from 4 OTDM channels

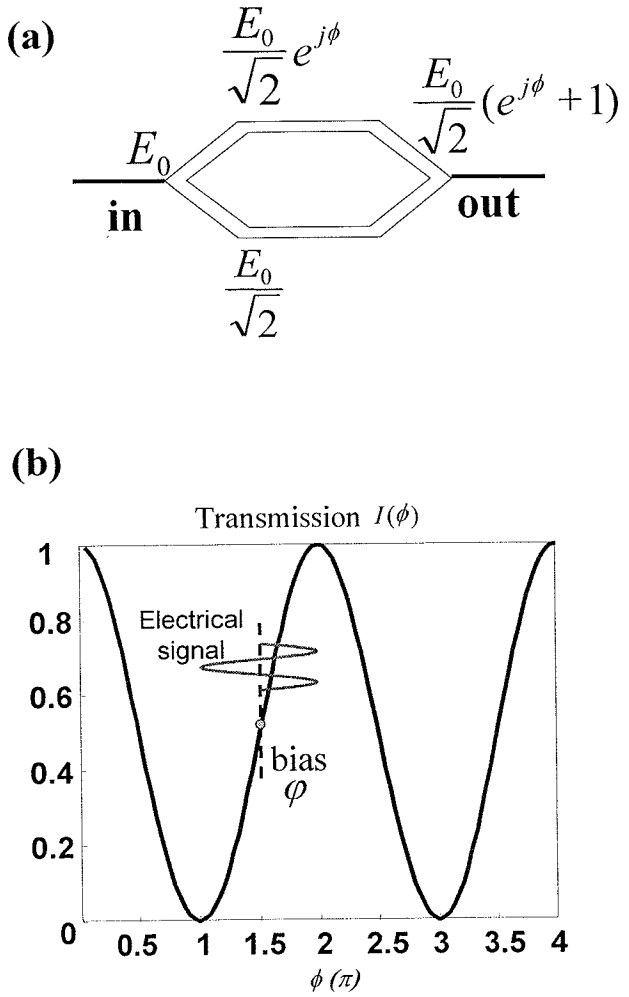

Fig. 4.11 Mach-Zehnder modulator: (a) structure: a phase difference ϕ between two tributaries. (b) transmission vs. ϕ. Electrical signal is added on phase ϕ to realize modulation.

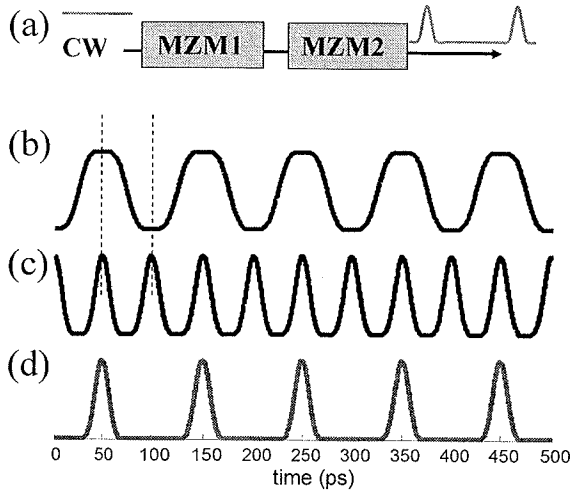

Fig. 4.12 Two Mach-Zehnder modulators to realize DEMUX: (a) structure (b) intensity modulation of the first MZM (c) intensity modulation of the second MZM (d) intensity modulation of the two MZM together.

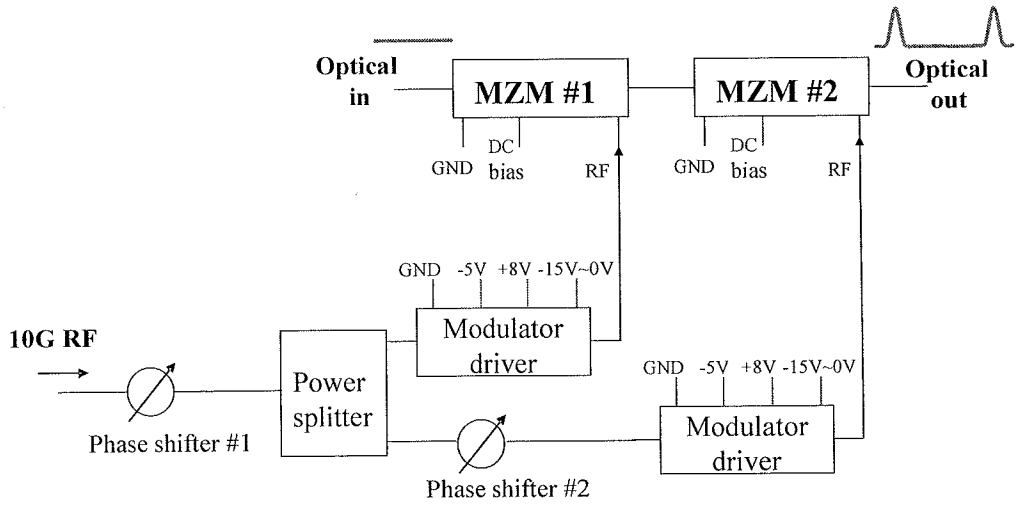

Fig. 4.13 The details of the DEMUX module.

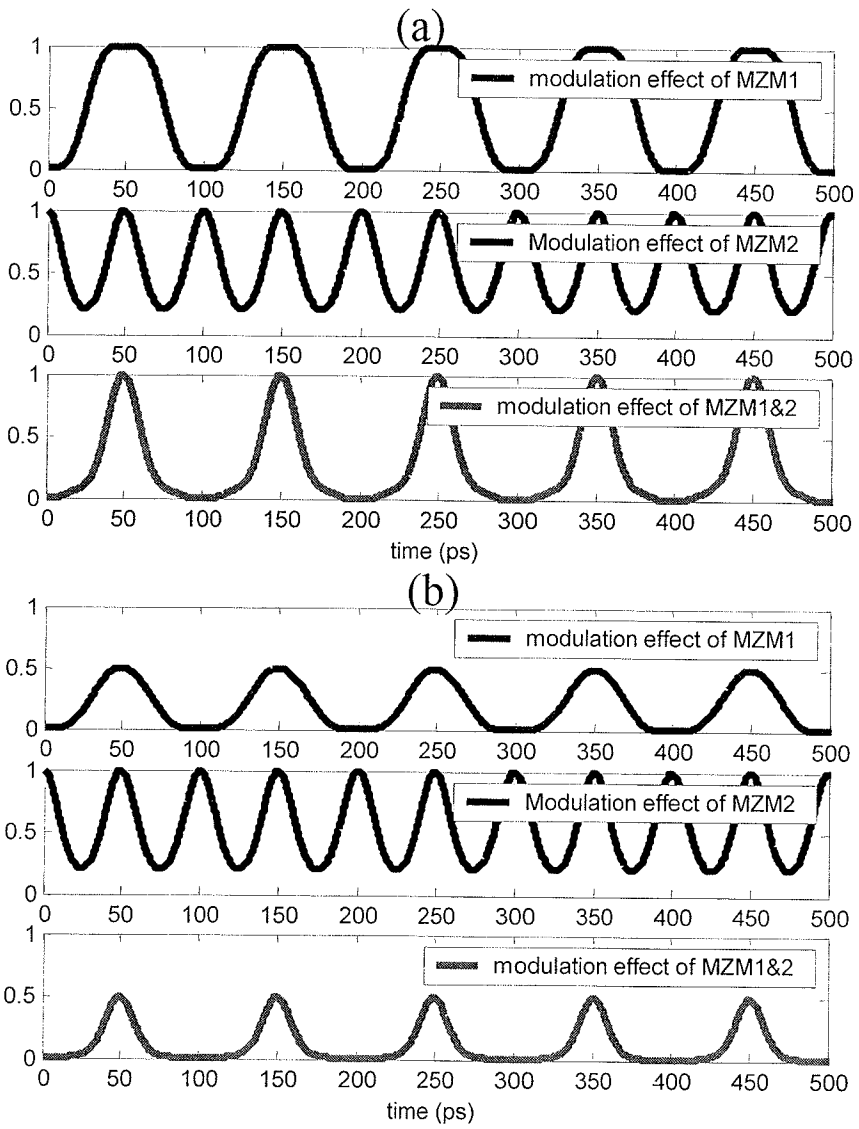

Fig. 4.14 The solution to overcome the RF drive limit in experiment to get better DEMUX time gate: (a) the problem: modulation of MZM2 does not have 0 valley, so the time gate (red) goes to zero slowly. (b) the solution: drive MZM1 to make the time gate goes to 0 quickly though introducing extra loss.

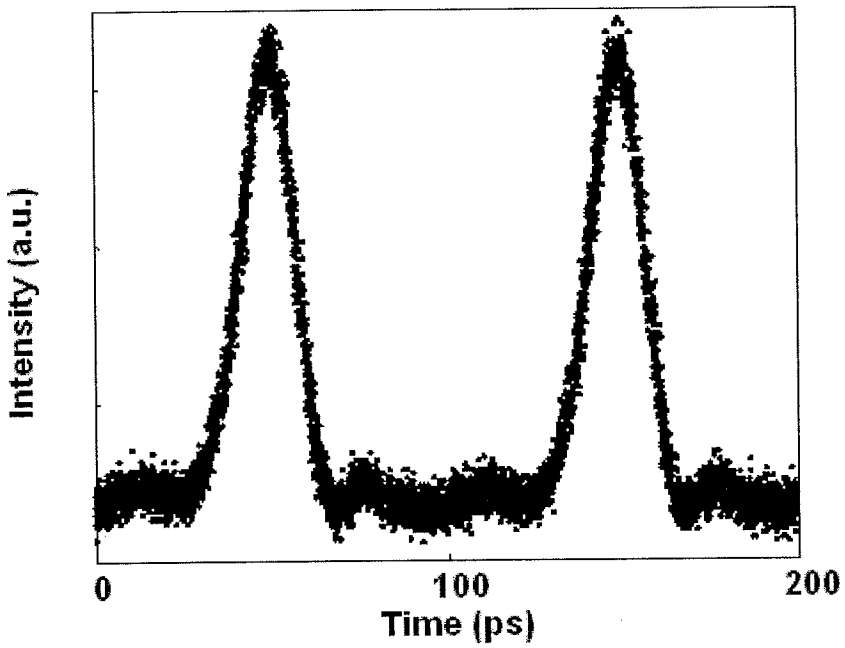

Fig. 4.15 The time gate of DEMUX on a fast scope (with a 50GHz photodiode).

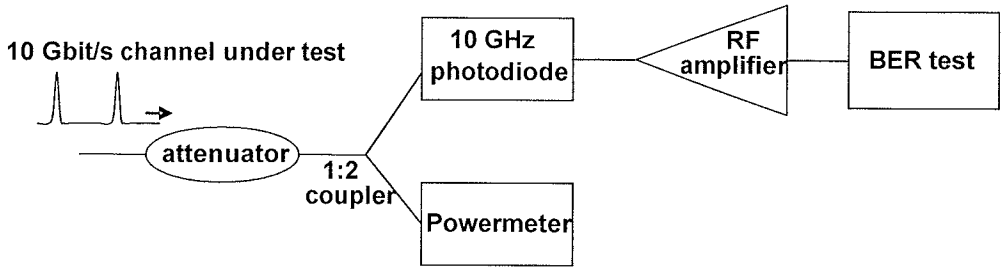

Figure 4.16 BER test structure.

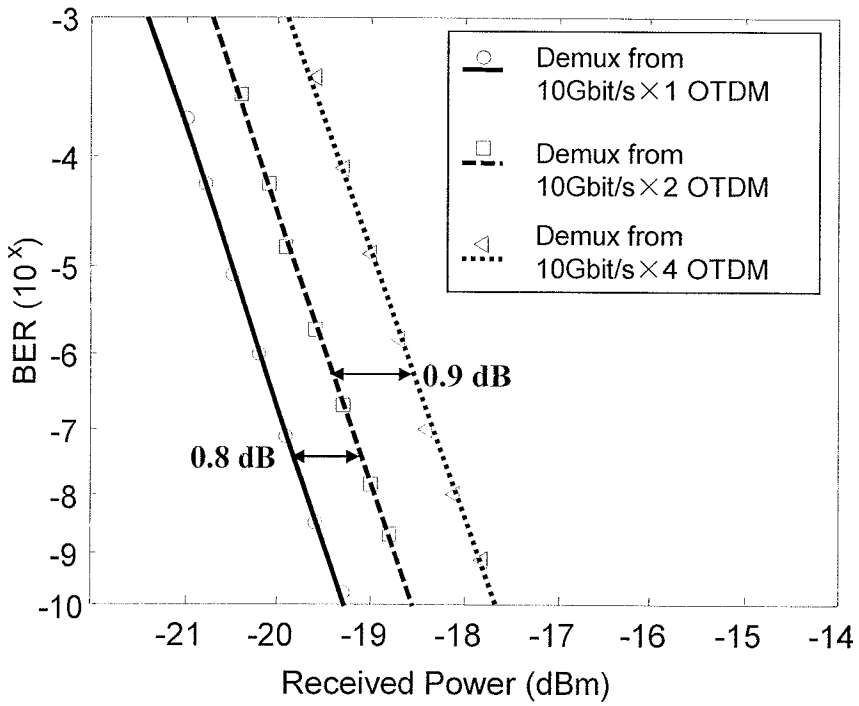

Fig. 4.17 Back-to-back BER test without PMD emulator and compensation. Solid line: demuxed from 10 Gbit/s×1 OTDM; Dash line: demuxed from 10 Gbit/s×2 OTDM; Dotted line: demuxed from 10 Gbit/s×4 OTDM

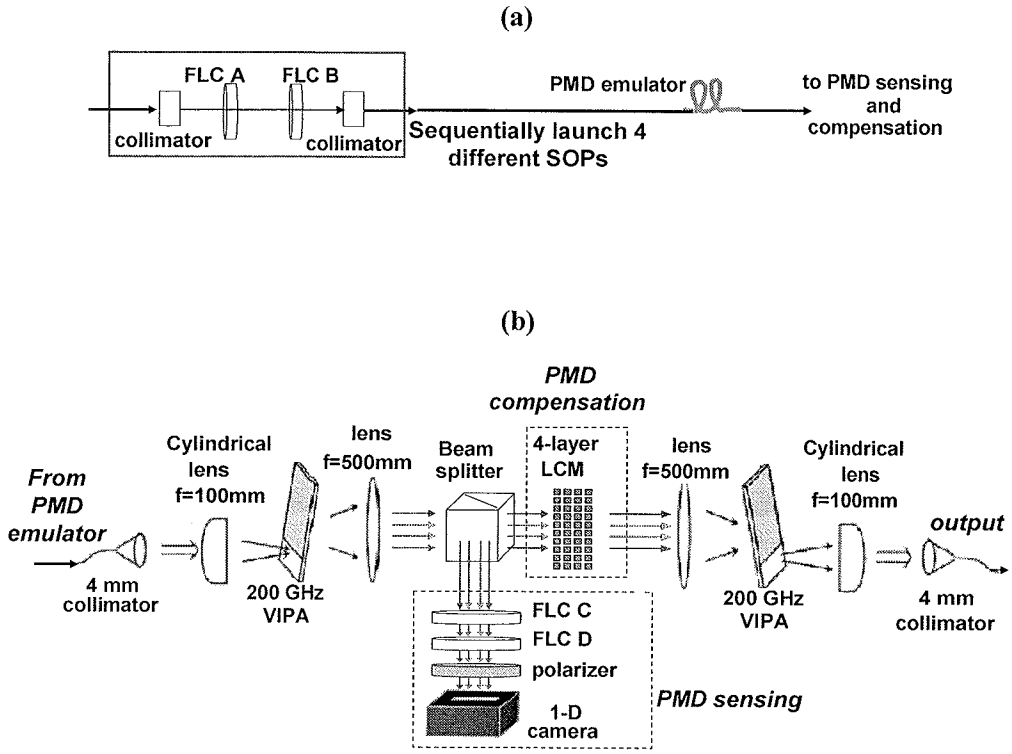

Fig. 4.18 (a) Sequentially launch 4 different SOPs to PMD emulator; (b) PMD sensing and compensation.

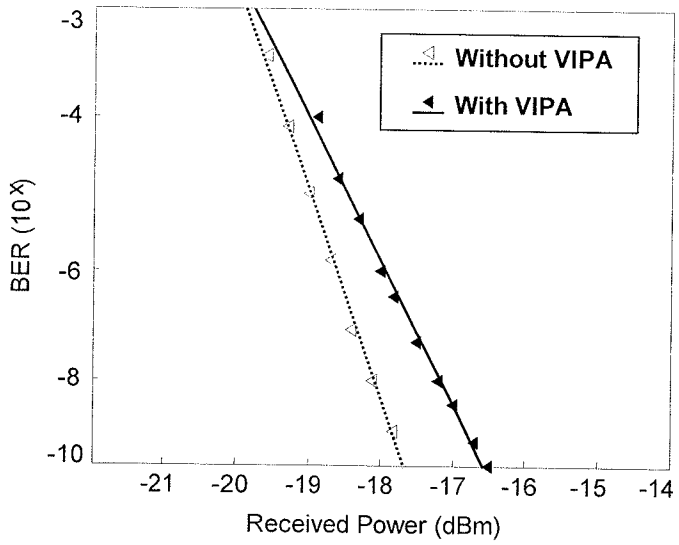

Fig. 4.19 Back-to-back BER test without PMD emulator for one channel demuxed from 10 Gbit/s×4 OTDM. Dotted line: without VIPA. Solid line: with VIPA (set for quiescent state)

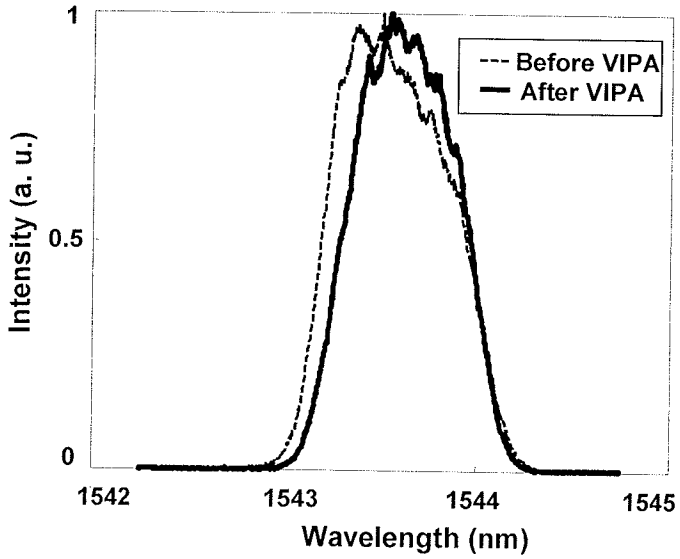

Fig. 4.20 Spetrum of the 10 Gbit/s×4 OTDM signal. Dashed line: before VIPA. Solid line: after VIPA.

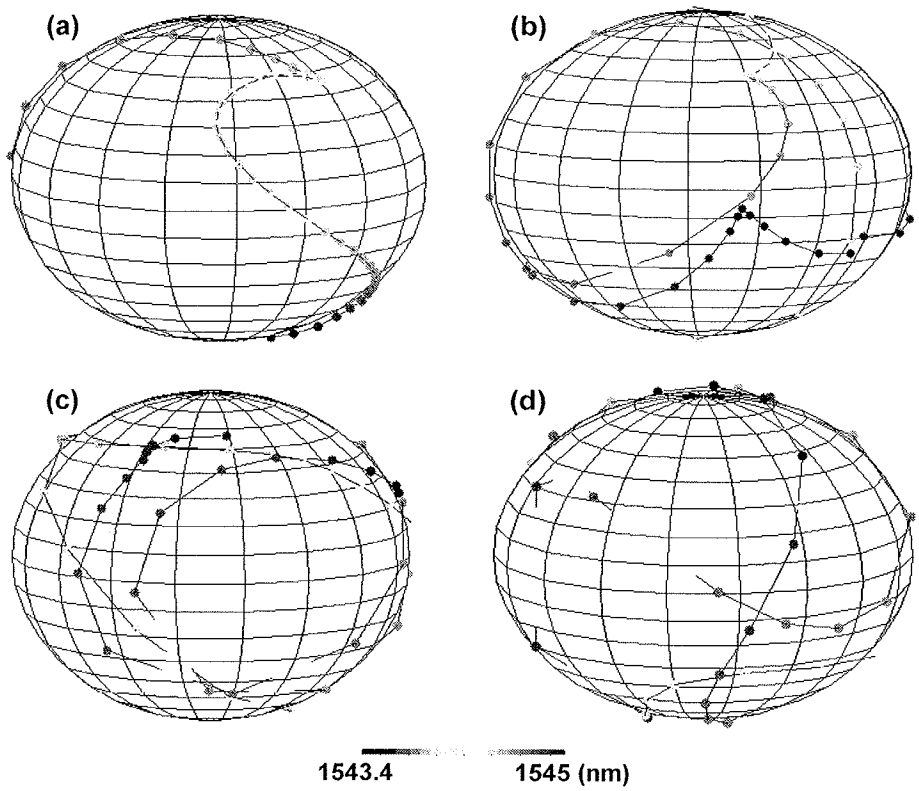

Fig. 4.21 Output SOP vs. wavelength for one launched SOP to four different emulators: (a) 29.1 ps mean DGD; (b) 45.3 ps mean DGD; (c) 57.5 ps mean DGD; (d) 58.8 ps mean DGD.

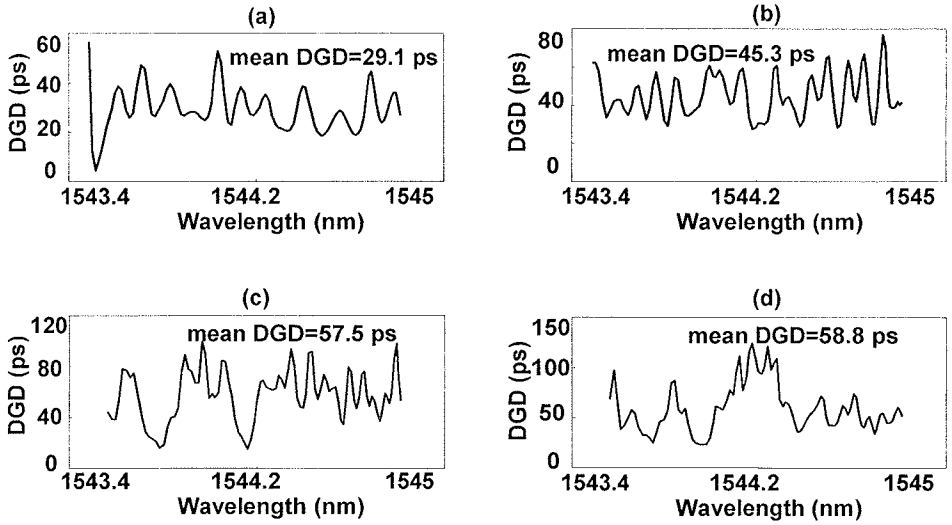

Fig. 4.22 DGD vs. wavelength: (a) 29.1 ps mean DGD; (b) 45.3 ps mean DGD; (c) 57.5 ps mean DGD; (d) 58.8 ps mean DGD.

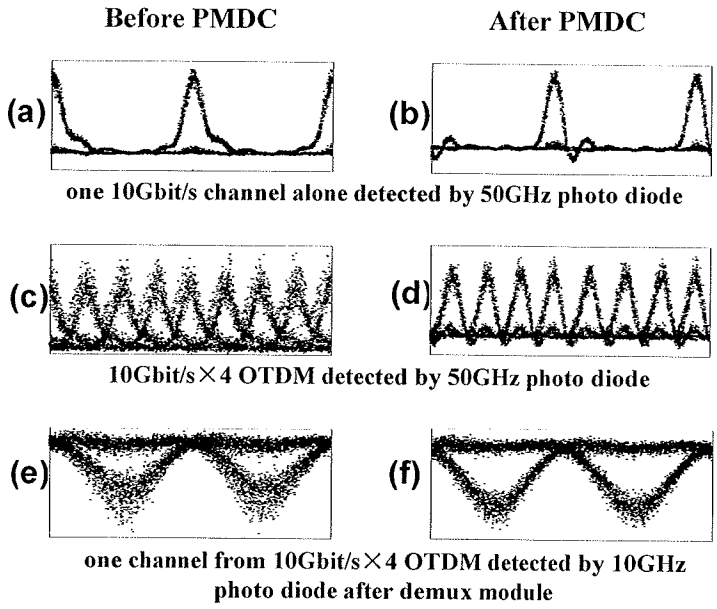

Fig. 4.23 Eye diagrams (200 ps time range) before and after PMDC (29.1 ps mean DGD).

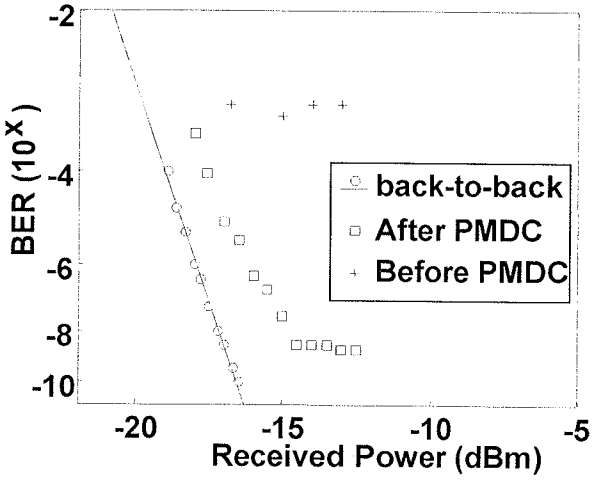

Fig. 4.24 BER of one channel demuxed from 10Gbit/s×4 OTDM before and after PMDC (29.1 ps mean DGD)

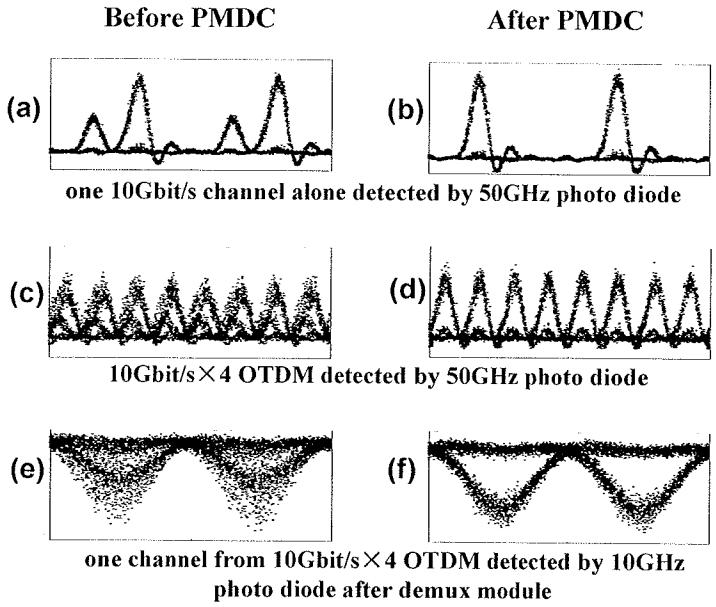

Fig. 4.25 Eye diagrams (200 ps time range) before and after PMDC (45.3 ps mean DGD).

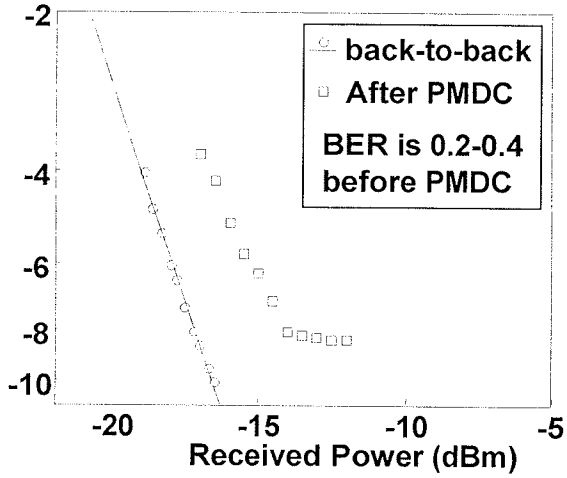

Fig. 4.26 BER of one channel demuxed from 10 Gbit/s×4 OTDM before and after PMDC (45.3 ps mean DGD)

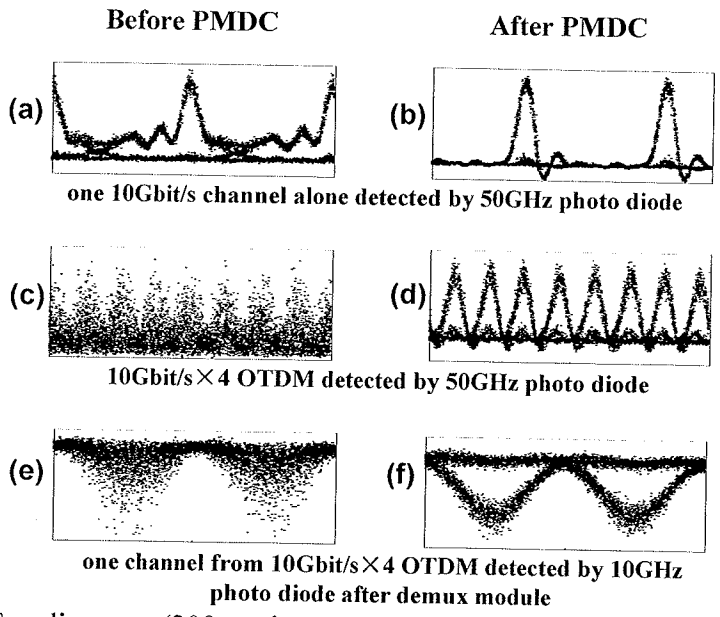

Fig. 4.27 Eye diagrams (200 ps time range) before and after PMDC (57.5 ps mean DGD).

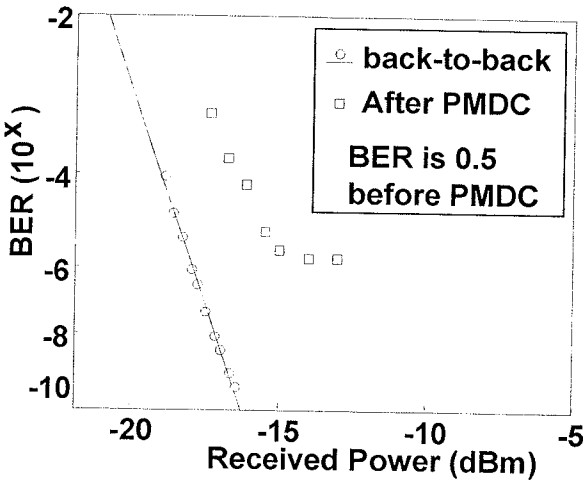

Fig. 4.28 BER of one channel demuxed from 10 Gbit/s×4 OTDM before and after PMDC (57.5 ps mean DGD)

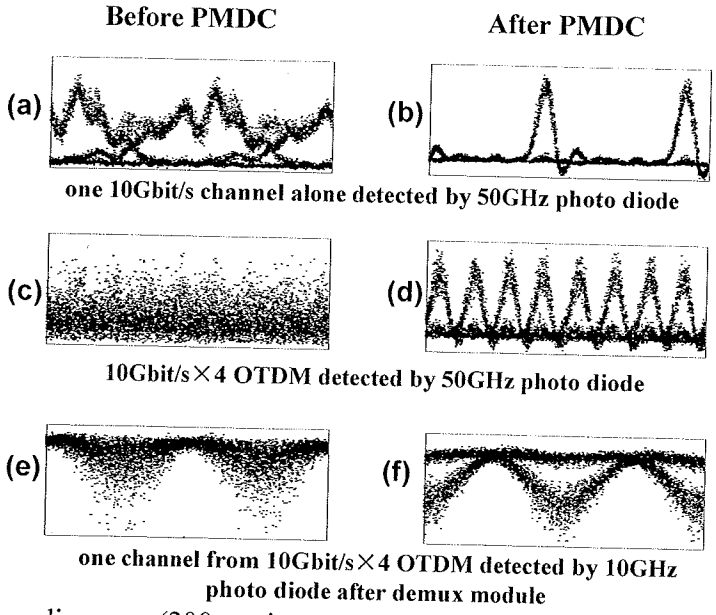

Fig. 4.29 Eye diagrams (200 ps time range) before and after PMDC (58.8 ps mean DGD).

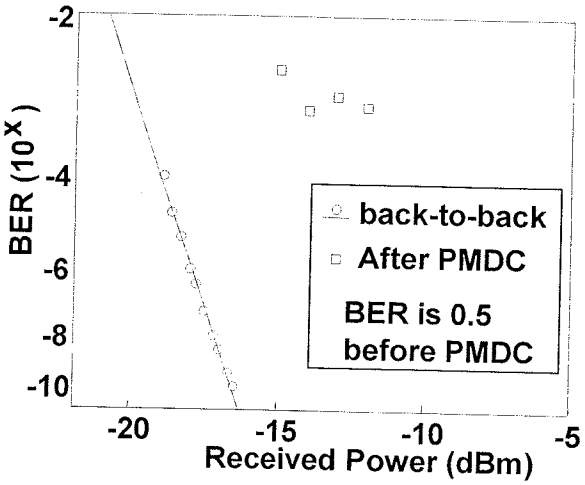

Fig. 4.30 BER of one channel demuxed from 10 Gbit/s×4 OTDM before and after PMDC (58.8 ps mean DGD)

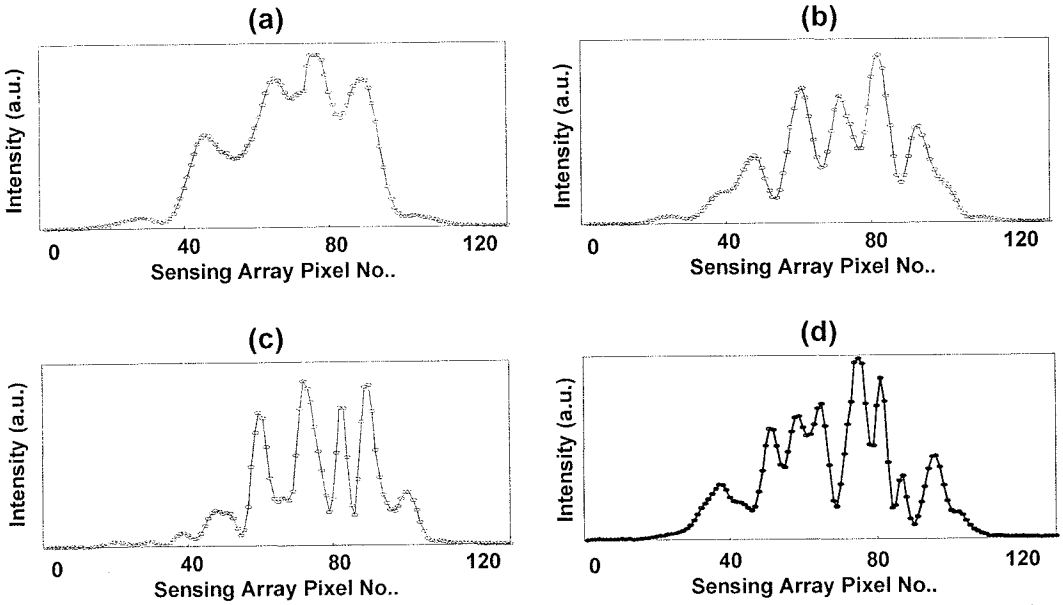

Fig. 4.31 The intensity of the 0° linear polarization component vs. pixel number (frequency) for a particular launch polarization into the emulator

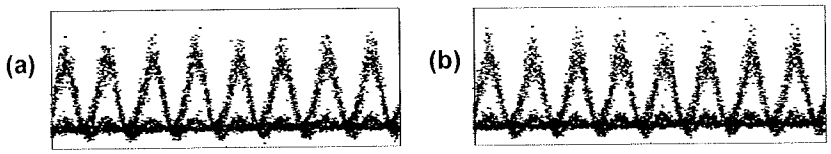

Fig. 4.32 Eye diagrams (200 ps time range) of 10 Gbit/s×4 OTDM. after PMDC. (a) with fixed input SOP to PMD emulator; (b) with input SOP to PMD emulator switching at 2 kHz between 0 and 90 degree linear SOP.

5. PMD COMPENSATION IN 10GBIT/S×2 POL-MUX SYSTEMS

Polarization division multiplexing (Pol-Mux) is an important method to improve spectral efficiency. For Pol-Mux used in ultrahigh-capacity fiber communication systems, Polarization mode dispersion (PMD) [3] not only distorts and broadens the signal, but also couples polarization-multiplexed channels. In the case of large (all-order) PMD, this coupling becomes strongly frequency-dependent. Moreover, PMD lowers Pol-Mux transmission tolerance to fiber nonlinearity and chromatic dispersion, making PMD compensation (PMDC) required [19]. Most research on PMDC, either electrical [44] or optical [45], has been limited to the first- or second-order PMD regime, which are valid only for distortions small compared to the bit period or pulse width. For the first time, we apply the technique of optical compensation of all-order PMD using a hyperfine resolution optical pulse shaper in a 10 Gbit/s × 2 Pol-Mux RZ (pulse width is ~9.4 ps FWHM) system. In this chapter, section 5.1 shows the experimental setup details, section 5.2 shows the PMD compensation results, and section 5.3 gives a brief conclusion.

5.1 Experimental Setup

Our experimental setup (shown in figure 5.1) begins with ~9.4 ps pulses (120 GHz bandwidth) spectrally sliced from a 10 GHz repetition rate mode-locked laser. Pulses are modulated at 10 Gbit/s using on-off keying. In addition, pseudorandom 0-π phase modulation is used for carrier suppression, which gives a spectrum more favorable for our PMD sensing scheme. The spectrum and the estimated pulse shape are shown in figure 5.2.

The signal then goes to polarization multiplexing module (details shown in figure 5.3). A polarization beam splits the signal into two channels: 0^0 and 90^0 linear polarization. On channel is delayed by exactly 8 symbols using mirror on a fine-tune translation stage. Then a polarization beam combiner combines two channels. We use

a polarization controller before the first beam splitter to adjust two channels for equal power.

A PMD emulator is constructed by concatenating over 10 polarization maintaining fiber sections with randomly set fast axes and different lengths. From our measurement [37] shown in figure 5.6, the differential group delay (DGD) vs. wavelength varies rapidly within the optical spectrum, covering a range from nearly zero to 110 ps with mean value of 41.5 ps.

The PMD sensing and compensation module is almost the same as in chapter 4. The difference is that only one input polarization channel is used in the sensing step. Because the degree of polarization (DOP) of 10 Gbit/s × 2 Pol-Mux signal is 0 and we cannot sense its SOP. After PMDC the signal is polarization demultiplexed back to 10G using a polarization controller and an in-line polarizer, as shown in figure 5.4. Then it is characterized using a 50 GHz photodiode and sampling scope, and 10 GHz photoreceiver and bit error rate test set.

We let the signal go through the whole system without PMD emulator and compensator, and test BER. We test the four cases: channel 1 alone, channel 2 alone, channel 1 and channel 2 demuxed from and each channel demuxed 10 Gbit/s × 2 Pol-Mux. As shown in figure 5.5, all BER for these 4 cases are close to each other. This shows that the system test bed for 10 Gbit/s × 2 Pol-Mux has high quality. Later we also perform back-to-back BER test with PMD compensator (set for quiescent state) as a baseline to compare PMDC results.

5.2 Experimental Results

The eye diagrams detected by a 50 GHz photodiode are shown in figure. 5.8. Figure 5.8 (a)-(e) is before PMDC. PMD severely distorts the original ~9.4 ps pulses, broadening them to over 100 ps (figure 5.8 (a) and (b)). Moreover, for each channel, the polarization vs. frequency traces show complicated trajectories on the Poincarè Sphere (one channel is shown in figure 5.7). Thus two Pol-Mux channels couple together and interfere severely as seen in figure 5.8 (c). After demultiplexing one channel from two, the eyes are closed, as seen in figure 5.8 (d)-(e). After PMDC the distorted signal is recovered, and the interference between channels is strongly reduced. Thus, prior to demultiplexing the eye for 10 Gbit/s×2 Pol-Mux exhibits three clear levels (at 0, 1, and 2), as is expected when these channels are uncoupled (figure 5.8 (h)).

Moreover, after demultiplexing, the eye for each channel is restored to excellent quality. BER test results for both channels after demultiplexing are shown in figure 5.9. We use the BER of the no-PMD case as back-to-back reference, which means the PMD emulator is taken out and the PMD compensation module is set for a quiescent state. With the emulator the bit error rate without PMD compensation is essentially 50%. After compensation, the BER is close to the no-PMD case, with almost no power penalty for Channel 1, and about 1.5 dB power penalty for Channel 2.

The degree of polarization (DOP) is 0 if two Pol-Mux channels have the same optical power. Thus for SOP sensing in this experiment, we only allow one channel to launch, and temporarily block the other. However, if we set the two channels for different power, say one has power 1 and the other has power r ($0<r<1$), we can measure SOP with DOP equal to $(1-r)/(1+r)$ when both channels are launched. This scheme may allow continuous PMD sensing for PMDC control during Pol-Mux transmission. Note that DOP decreases as r increases towards one, which reduces OSNR for SOP sensing, while small r will lead to low OSNR transmission for one of the channels. Therefore, an appropriate value of r will involve a trade-off between these factors.

5.3 Conclusions

We experimentally demonstrate feed-forward all-order optical PMD compensation in a 10 Gbit/s×2 Pol-Mux 10% RZ system with large PMD (mean DGD >40ps) using a hyperfine resolution pulse shaper provisioned with a four-layer liquid crystal modulator array and frequency-dependent Jones matrix sensing. The short pulse source we used here indicates that this approach may be extended to 40 Gbit/s×2 Pol-Mux or higher symbol rate.

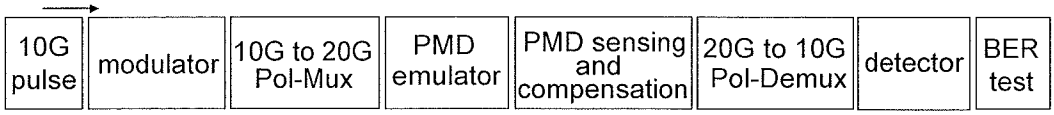

Fig. 5.1 The full experimental setup.

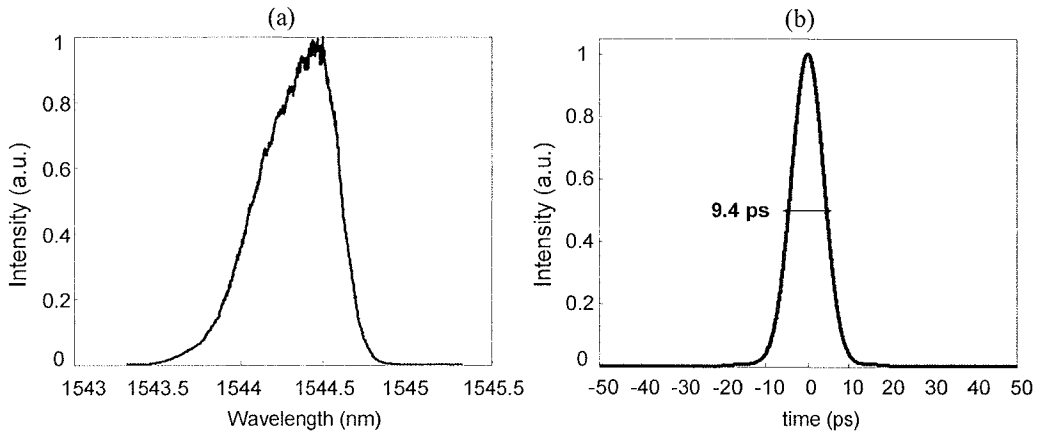

Fig. 5.2 (a) spectrum of 10 Gbit/s signal with carrier suppression; (b) estimated pulse shape (9.4 ps FWHM) by performing FFT on the spectrum in (a).

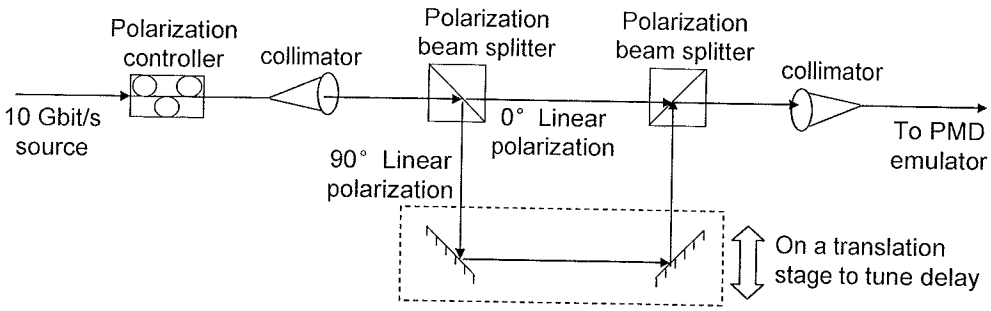

Fig. 5.3 10G-to-20G polarization multiplexer.

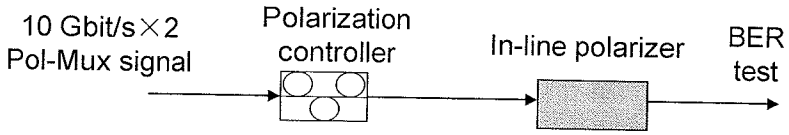

Fig. 5.4 20G-to-10G polarization demultiplexer.

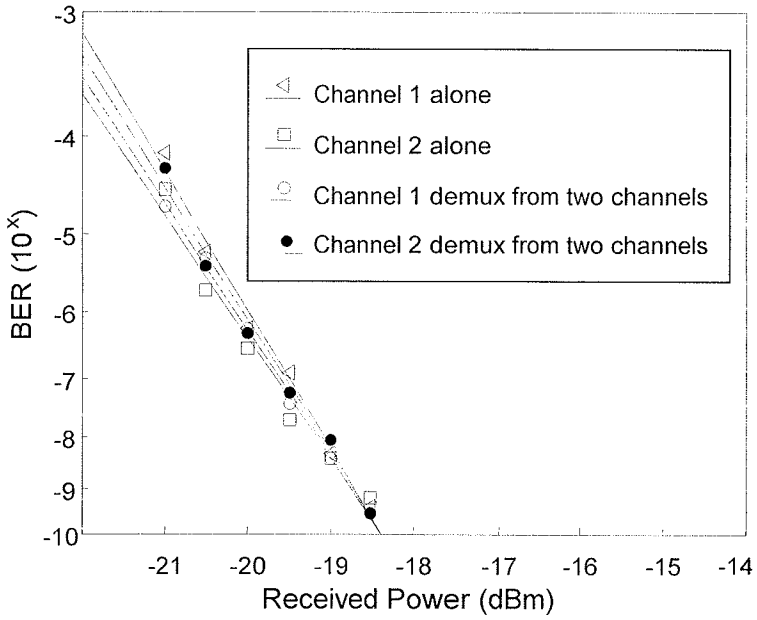

Fig. 5.5 BER test results for testing Pol-Mux and Pol-Demux. Triangle: channel 1 alone; Square: channel 2 alone; Circle: channel 1 demux from two channels; Dot: channel 2 demux from two channels.

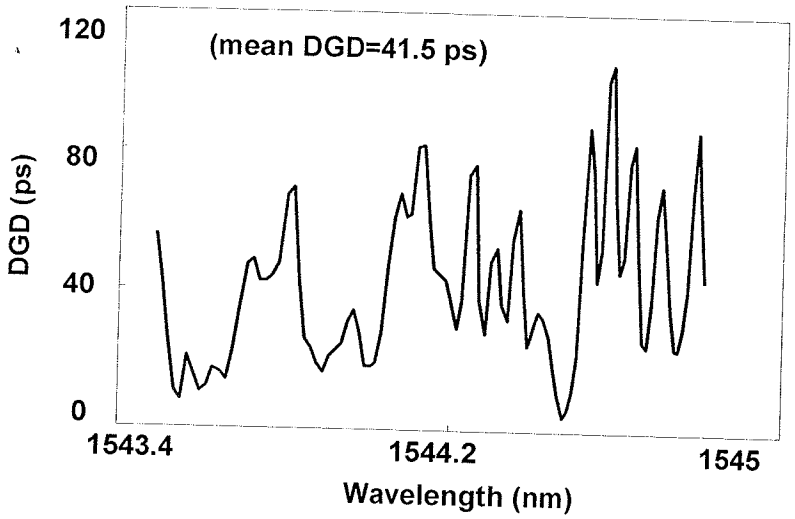

Fig. 5.6 DGD vs. wavelength for the PMD emulator.

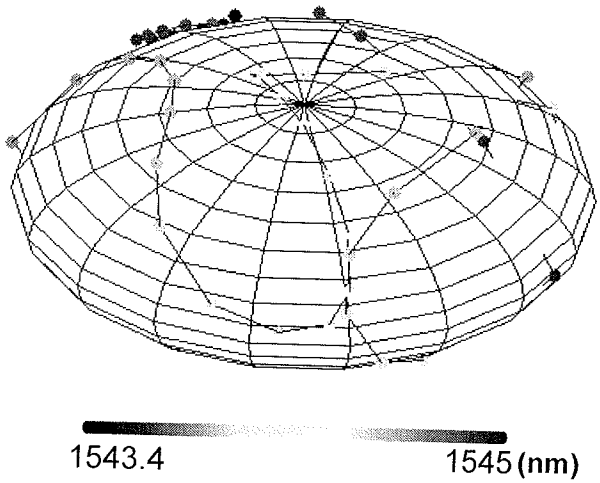

Fig. 5.7 Output state of polarization vs. wavelength of one Pol-Mux channel after PMD emulator.

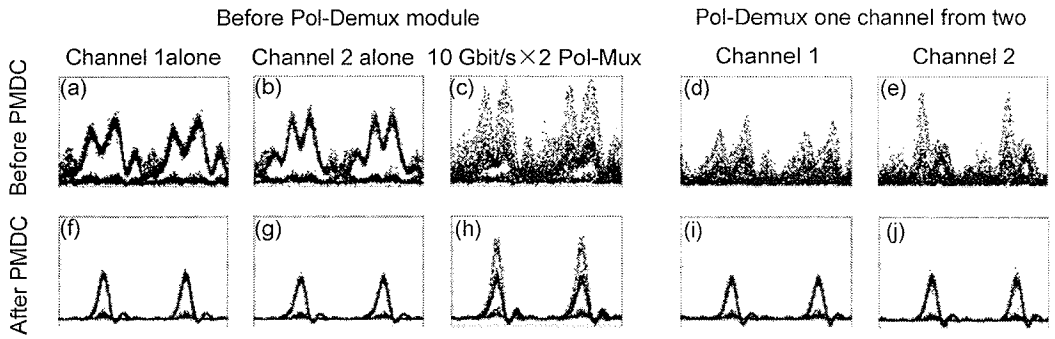

Fig. 5.8 Eye diagrams (200 ps time range) arranged in 2 rows and 5 columns. Rows: the first row is before PMDC ; the second row is after PMDC ; Columns: the first three columns are grabbed before Pol-Demux module for channel 1, channel 2 and two channels muxed together; the last two columns are grabbed after Pol-Demux for channel 1 and channel 2.

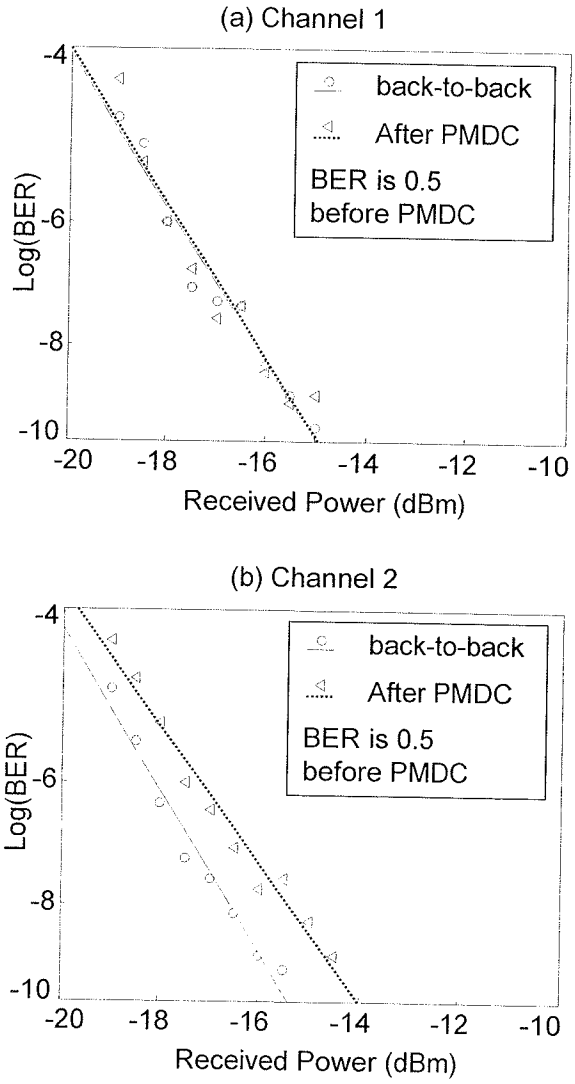

Fig. 5.9 BER test results for each channel after demuxed from 10 Gbit/s×2 Pol-Mux:(a) Channel 1; (b) Channel 2.

6. SUMMARY AND FUTURE DIRECTIONS

We experimentally apply a unique high-speed spectral polarimeter to realize near-real-time all-order broadband Polarization Mode Dispersion (PMD) measurements. Furthermore, for the first time we apply the technique of all-order PMD compensation via hyperfine resolution optical pulse shaping in optical fiber communication system experiments: (1) 40 Gbaud/s systems; (2) 10 Gbit/s×2 Pol-Mux systems.

There are several possible directions in the future:

(1) Our all-optical PMD compensation approach can be readily extended to higher symbol rates, 80 Gbaud/s or even for those with pulses down to the sub-ps range [18]. For higher symbol rate signal, because the bandwidth is larger, with the same amount of PMD, the higher order PMD effect becomes more significant. This makes our all-order PMD compensation scheme more advanced than other schemes. To implement such an experiment with symbol rate 80 Gbaud/s or above, the direct RF modulation may not feasible, thus OTDM is still a reasonable choice. The 200 GHz VIPA band is just sufficient for 80 Gbaud/s realized by OTDM. For 160 Gbaud/s, the pulse shaping of a larger band is needed.

(2) Consider polarization dependent loss (PDL) effect in our PMD compensation scheme. Polarization dependent loss means that light in different SOP traveling through a material experiences various losses. Many optical components introduce PDL, for example, optical fibers, couplers, multiplexers/demultiplexers, combiners/splitters, and EDFAs [46]. Polarization dependent loss and polarization mode dispersion vary randomly along the transmission line and they interact with each other. As a result, the system degradation is not just a simple addition of both effects [47]. Analytically, people use stochastic dynamic equations to study the cross effect between PDL and PMD [47, 48, 49]. These complex analyses induce some simple facts: (a) With PDL, two principal states of polarization are not orthogonal. (b) PMD is enhanced with the presence of PDL. (c) PMD correlation bandwidth is reduced with PDL. These indicate that PDL should be considered in PMD effect. Some group experimentally studied PDL effect in optical domain PMD compensation [50], and shows that for first and second

order PMD compensation in a 10 Gb/s system with 24~44 ps DGD, even 0.5dB PDL seriously limits the system performance. The PDL effect on our all-order PMD compensation scheme is yet to study. Polarization dependent loss does exist in our PMD emulator made by high birefringence polarization maintaining fiber, according to a research on the PDL effects in PMD emulators [51]. However, we assume no PDL in our PMD monitoring and compensation. The excellent compensation results indicate that our scheme has certain tolerance to PDL. This raises several questions: How large is this tolerance? How does PDL affect our all-order PMD compensation? If PDL exceeds the tolerance, is there any improvement on the PMD compensation scheme? This research may be performed in two parts: (a) Simulation to help the analysis on the PDL effects in PMD sensing and compensation, and to find possible algorithms for improvement. (b) Experiments on PDL effect analysis, and to demonstrate the improved algorithms.

(3) Make our PMD compensation approach practical for deployment in actual systems. We need to automate the PMD sensing and compensation, so that the compensation is seamless and endless. We also need to reduce the PMDC time to milliseconds scale (PMD of a system varies occasionally in this time scale [2]) by using higher speed modulator arrays, because the current LCM layers have response time of about tens of milliseconds [52]. There are also some other concerns such as how to realize compact size and low cost. Currently in industry the most popular solution for the on-going 40/100 Gbit/s systems is Dual-Polarization QPSK format with polarization diversity coherent detection and digital signal processing [53]. The advantages are as follows: (a) It fits into current network infrastructure with 50GHz ITU (International Telecommunication Union) grid. (b) The symbol rate is not too high for the transmitter and receiver hardware, because the ultra-high speed electronics is not available today. (c) By digital signal processing after polarization diversity coherent detection, Pol-Mux channels are demuxed, and both PMD and chromatic dispersion are compensated. As for our VIPA based hyperfine resolution optical pulse shaping, besides PMD compensation (works well on Pol-Mux too), it can also perform chromatic dispersion compensation [54]. The biggest advantage of our approach is that PMDC ability should scale to high symbol rates (40 Gbaud/s and beyond). Therefore, it may have larger potential for the future 200Gbit/s systems and beyond.

LIST OF REFERENCES

LIST OF REFERENCES

[1] Greg Raybon and Peter J. Winzer, "100G Challenges and Solutions", in *2008 Optical Fiber Communications Conference (OFC2008)*, San Diego, CA, February 24-28, 2008

[2] Magnus Karlsson, Jonas Brentel, and Peter A. Andrekson, "Long-Term Measurement of PMD and Polarization Drift in Installed Fibers", *Journal of Lightwave Technology*, Vol. 18, No. 7, pp. 941-951, Jul. 2000

[3] Herwig Kogelnik, Robert M. Jopson, and Lynn E. Nelson, "Polarization-Mode Dispersion", *Optical Fiber Telecommunications*, Volume IVB, Chapter 15, Elsevier Science, pp. 725-860, 2002

[4] Reza Khosravani, "Polarization mode dispersion compensation in optical and electrical domain and their limitations", *Opt. Eng*, Vol.43, No. 5, pp. 1035-1041, May. 2004.

[5] C.D. Poole, and David L. Favin, "Polarization-Mode Dispersion Measurements Based on Transmission Spectra Through a Polarizer", *Journal of Lightwave Technology*, Vol. 12, No. 6, pp. 917-929, June, 1994

[6] B.L. Heffner, "Automated Measurement of Polarization Mode Dispersion Using Jones Matrix Eigenanalysis", *Photonics Tech. Lett.*, Vol.4, No. 9, pp. 1066-1069, 1992

[7] R.M. Jopson, "Measurement of Second-Order Polarization-Mode Dispersion Vectors in Optical Fibers", *Photnonics Tech. Lett.*, Vol.11, No.12, pp. 1153-1155, 1999

[8] C. D. Poole, Neal. S. Bergano, R. E. Wagner, and H. J. Schulte, Polarization Dispersion and Principal States in a 147-km Undersea Lightwave Cable", *Journal of Lightwave Technology*, Vol.6, No.7, pp. 1185-1190, July 1988

[9] P. B. Phua, and Hermann A. Haus, "All-Frequency PMD Compensator in Feedforward Scheme", *Journal of Lightwave Technology*, Vol. 22, No.5, pp. 1280-1289, May 2004

[10]X. Wang and A.M. Weiner, "Fast Wavelength-parallel polarimeter for broadband optical networks", *Optics Letters*, Vol. 29, No. 9, pp. 923-925, 2004

[11]Li Xu, Houxun Miao and Andrew M. Weiner, "Fast Measurement of Polarization Mode Dispersion via Virtually Imaged Phased-Array Based Spectral Polarimetry", in *2008 Optical Fiber Communications Conference (OFC2008)*, San Diego, CA, Feb. 24-29, 2008.

[12]R. Noè, "PLL-Free Synchronous QPSK Polarization Multiplex/Diversity Recovery Concept With Digital I&Q Baseband Processing", *IEEE Photonics Technology Letters*, Vol. 17, No. 4, pp. 887-889, April. 2005.

[13]L. E. Nelson, S. L. Woodward, and etc., "Performance of a 46-Gbps Dual-Polarization QPSK Transceiver in a High-PMD Fiber Transmission Experiment", in *2008 Optical Fiber Communications Conference (OFC2008)*, San Diego, CA, post-deadline paper section, Feb. 24-29, 2008.

[14]T. Ono, Y. Yano, L. D. Garrett, J. A. Nagel, M. J. Dickerson, and M. Cvijetic, "10Gb/s PMD compensation field experiment over 452km using principal state transmission method", in *Tech. Digest of Optical Fiber Communication Conf. (OFC'00)*, 2000.

[15]Qian Yu and A. E. Willner, "Comparison of optical PMD compensation using a variable and fixed differential group delays", *Optical Fiber Communication Conference (OFC)*, Anaheim, California, March 17, 2001

[16]H. Miao, A. M. Weiner, L. Mirkin and P. J. Miller, "All-Order Polarization Mode Dispersion Compensation (PMD) via Virtually Imaged Phased-Array (VIPA) Based Pulse Shaper," *IEEE Photonics Technology Letters*, Vol. 20, No. 8, pp. 545-547, Apr. 2008.

[17]M. Shirasaki, "Large Angular Dispersion by a Virtually Imaged Phased Array and its Application to a Wavelength Demultiplexer," *Optics Letters*, vol.21, pp.366–368, March 1996

[18]H. X. Miao, A. M. Weiner, L. Mirkin, and P. J. Miller, "Broadband All-Order Polarization Mode Dispersion Compensation via Wavelength-by-Wavelength Jones Matrix Correction," *Optics Letters*, Vol. 32, pp. 2360-2362, August 2007

[19]D. van den Borne, N. E. Hecker-Denschlag, G. D. Khoe, and H. de Waardt, "PMD-induced transmission penalties in polarization-multiplexed transmission" *Journal of Lightwave Technology*, Vol. 23, No. 12, pp. 4404-4015, Dec. 2005

[20]C. L. Chen, *Elements of Optoelectronics & Fiber Optics,* Chapter 10, Richard D. Irwin, a Times Mirror Higher Education Group, Inc. company, pp. 533-583, 1996.

[21]W. A. Shurcliff, "Modern Description of Polarized Light", *Polarized Light, Production and Use*, Harvard University Press, pp. 15-31, 1996.

[22]Mehmetcan Akbulut, *Broadband All order Polarization Mode Dispersion Compensation Using Liquid-Crystal Modulator Arrays*, Ph.D. thesis, ECE Dept. at Purdue University, Aug. 2005

[23]C. L. Chen, *Elements of Optoelectronics & Fiber Optics*, Chapter 8, Richard D. Irwin, a Times Mirror Higher Education Group, Inc. company, pp. 437-472, 1996.

[24]F. Heismann, "Polarization Mode Dispersion: Fundamentals and Impact on Optical Communication Systems", Tutorial, Presented at *European Conference on Optical Communications*, Sep. 1998.

[25]N. Gisin and J. P. Pellaux, "Polarization mode dispersion: time versus frequency domains", *Optics Communications 89* (1992) North-Holland, pp. 316-323

[26]C. D. Poole and R. E. Wagner, "Phenomenological approach to Polarization dispersion in long single-mode fibers," *Electron. Lett.*, Vol.22, pp. 1029-1030, 1986

[27]G. J. Foschini, and C.D. Poole, "statistical Theory of Polarization Dispersion in Single Mode Fibers", *Journal of Lightwave Technology*, Vol. 9, pp. 1439-1455,Nov, 1991

[28]J. P. Gordon and H. Kogelnik, "PMD fundamentals: Polarization mode dispersion in optical fibers," *Proc. Nat. Acad. Sci.*, Vol. 97, No. 9, pp. 4541-4550, Apr. 25, 2000.

[29]H. Bülow, "Limitation of optical first-order PMD compensation," *Optical Fiber Communication Conf. 1999/Int. Conf. Integrated Optics and Optical Fiber Communication. (OFC/IOOC '99) Tech. Dig.*, vol. 2, pp.74–76, 1999

[30]S. X. Wang and A. M. Weiner, "A Complete Spectral Polarimeter Design for Lighwave communication Systems," *Journal of Lightwave Technology*, Vol. 24, No.11, pp. 3982-3991, Nov. 2006.

[31]S. X. Wang, A. M. Weiner, S.-H. Foo, D. Bownass, M. Moyer, M. O'Sullivan, M. Birk, and M. Boroditsky, "PMD Tolerance Testing of a Commercial Communication System Using a Spectral Polarimeter," *Journal of Lightwave Technology*, Vol. 24, No. 11 , pp. 4120-4126, Nov. 2006.

[32]M. Boroditsky, K. Cornick, C. Antonelli, M. Brodsky, S. D. Dods, N. J. Frigo, and P. Magill, "Comparison of system penalties from first and multi-order PMD," *IEEE Photon. Technol. Lett.*, vol. 17, no. 8, pp. 1650–1652, Aug. 2005.

[33]M. Akbulut, A. M. Weiner, and P. J. Miller, "Wideband All-Order Polarization Mode Dispersion Compensation via Pulse Shaping," *Optics Letters*, Vol. 30, No. 20, pp. 2691-2693, Oct. 2005.

[34]Li Xu, *Polarization Mode Dispersion Analysis Via Spectral Polarimetry and High-Order Correlations*, M.S.E.E. thesis, ECE Dept. at Purdue University, Aug. 2006

[35]S.X. Wang, S. Xiao, and A.M. Weiner, "Broadband, High Spectral Resolution 2-D Wavelength-Parallel Polarimeter for Dense WDM Systems", *Optics Express*, Vol.13, 9374-9380, Nov. 2005.

[36]S. Xiao, A.M. Weiner, and C. Lin, "A dispersion law for virtually imaged phased-array spectral dispersers based on paraxial wave theory," *IEEE Journal of Quantum Electronics*, Vol. 40, No. 4, pp. 420-426, April 2004

[37]Li Xu, Shawn X. Wang, Houxun Miao, and Andrew M. Weiner, "Polarization mode dispersion spectrum measurement via high-speed wavelength-parallel polarimetry", *Applied Optics*, Vol. 48, Iss. 24, pp. 4688–4697, 2009

[38]S. T. Lagerwall, *Ferroelectric and Antiferroelectric Liquid Crystals* (Wiley–VCH,New York, 1999).

[39]A. T. Clausen, H.N. Poulsen, and etc. "Pulse requirements for OTDM systems", *LEOS 2003*, 2003

[40]C.-B. Huang, Z. Jiang, D. E. Leaird, and A. M. Weiner, "High-Rate Femtosecond Pulse Generation via Line-by-Line Processing of a Phase-Modulated CW Laser Frequency Comb," *Electronics Letters*, Vol. 42, pp. 1114-1115, 2006.

[41].Peter J. Winzer and Renè-Jean Essiambre, "Advanced Optical Modulation Formats", *Proceedings of the IEEE*, Vol. 94, No. 5, May 2006

[42]C.B. Huang, S.G. Park, D.E. Leaird, and A.M. Weiner, "Nonlinearly Broadened Phase-Modulated Continuous-Wave Laser Frequency Combs Characterized using DPSK Decoding," *Optics Express,* Vol.16, 2520-2527, 2008.

[43].Houxun Miao, *All-Order Polarization Mode Dispersion Compensation*, Ph.D. thesis, ECE Dept. at Purdue University, Aug. 2008

[44]Noriaki Kaneda, and Andreas Leven, "Coherent polarization-division-multiplexed QPSK receiver with fractionally spaced CMA for PMD compensation", *IEEE Photonics Technology Letters*, VOL. 21, No. 4, pp. 203-205, Feb. 2009

[45] Yunfeng Shen, Xiumin Liu, Shan Zhong, John Veselka, Peter Kim, Michael Frankel, and Harshad Sardesai, "PMDC for polarization multiplexed RZ-DQPSK systems", *OFC 2009*, March 2009, San Diego, CA, U.S.A.

[46] Liang Chen, Saeed Hadjifaradji, David S. Waddy and Xiaoyi Bao, "Effect of local PMD and PDL directional correlation on the principal state of polarization vector autocorrelation", *Optics Express*, vol. 11, No. 23, pp. 3141-3146, Nov. 2003

[47] N. Gisin, B. Huttner, " Influence of polarization dependent loss on birefringent optical fiber networks", presented at *OFC'2000*, Baltimore, U.S.A. 2000.

[48] Y. Li and A. Yariv, "Solutions to the dynamical equation of polarization-mode dispersion and polarization-dependent losses," *J. Opt. Soc. Am. B*, Vol.17, pp. 1821-1827, 2000.

[49] Ricardo Feced, Seb J. Savory, and Anagnostis Hadjifotiou, "Interaction between polarization mode dispersion and polarization-dependent losses in optical communication links", *J. Opt. Soc. Am. B*, Vol. 20, No. 3, pp. 424-433, March 2003.

[50] Na Young Kim, Duckey Lee, Namkyoo Park and ect., "Limitation of PMD Compensation Due to Polarization-Dependent Loss in High-Speed Optical Transmission Links", *IEEE Photonics technology letters*, Vol. 14, No. 1, pp. 104, 2002

[51] A. Bessa dos Santos and J. P. von der Weid, "PDL Effects in PMD Emulators Made Out With HiBi Fibers: building PMD/PDL Emulators", *IEEE photonics technology letters*, Vol. 16, No. 2, pp. 452-454, Feb. 2004.

[52] A. M. Weiner, D. E. Leaird, J. S. Patel, and J. R. Wullert, "Programmable femtosecond pulse shaping by use of a multielement liquid-crystal phase modulator," *Optics. Letters.*, vol. 15, pp. 326-328, 1990

[53] Bernd Nebendahl (Agilent Technologies), "Metrology of Advanced Optical Modulation Formats for 40/100G and beyond", *IEEE Comunications online Tutorial*, April 2010.

[54] G.-H. Lee, Z. Jiang, S. Xiao and A.M. Weiner, "1700 ps/nm tunable dispersion compensation for 10 Gbit/s RZ lightwave transmission", *Electronic Letters*, Vol.42, No. 13, pp768-770., June 2006

VITA

VITA

Li Xu received her B.S. degrees from the Department of Electronics Engineering, Tsinghua University, Beijing, China, in 2002. She received M. S. E. E. degree from the Department of Electrical and Computer Engineering, Purdue University, West Lafayette, IN, in 2006. She is currently a Ph.D. candidate in the School of Electrical and Computer Engineering at Purdue University, West Lafayette, IN.

Her research focuses on the areas of all-order polarization mode dispersion sensing and compensation in optical fiber communication systems. She has been author or co-author of over 10 journal articles and conference papers.